IGHV3-53 antibody abundance drives divergent SARS-CoV-2 immune imprinting

Xiao Niu[1,2,3,#], Fanchong Jian[1,#], Yutong Li[1,2], Ke Li[1,2], Siyu Lei[1,2,4], Weiliang Song[1,2], Ruoxi Kong[1,2], Xingan Cai[1,2], Ran An[2], Yao Wang[2], Yifei Huang[5,6,7], Lingling Yu[2], Wenjing Wang[2], Haiyan Sun[2], Yuanling Yu[2], Jing Wang[2], Binmao Zhang[8], Tianen Zhu[8,9], Jianheng Huang[8,10], Fei Shao[2], Xiaotian Tan[8], Sai Luo[5,6,7], Yunlong Cao[1,2,4*]

[1]Biomedical Pioneering Innovation Center (BIOPIC), School of Life Sciences, Peking University, Beijing, P.R. China.

[2]Changping Laboratory, Beijing, P.R. China.

[3]College of Chemistry and Molecular Engineering, Peking University, Beijing, P.R. China.

[4]Peking–Tsinghua Center for Life Sciences, Peking University, Beijing, P. R. China.

[5]Center for Infectious Disease Research, Tsinghua University, Beijing, P.R. China.

[6]Tsinghua-Peking Joint Center for Life Sciences, Tsinghua University, Beijing, P.R. China.

[7]School of Basic Medical Sciences, Tsinghua University, Beijing, P.R. China.

[8]Shenzhen Institutes of Advanced Technology, Chinese Academy of Sciences.

[9]Shenzhen University General Hospital.

[10]Shenzhen University.

[*]Correspondence: Yunlong Cao (yunlongcao@pku.edu.cn).

[#]These authors contributed equally.

Abstract:

The mechanisms driving divergent SARS-CoV-2 immune imprinting in populations primed with different COVID-19 vaccines remain unclear. Recipients of inactivated vaccines readily develop Omicron-specific antibodies through repeated breakthrough infections, whereas mRNA-vaccinated individuals exhibit severe ancestral-strain imprinting that suppresses *de novo* Omicron-specific responses. These differences could result in distinct antibody landscapes, leading to regional epidemiological divergence and necessitating region-specific vaccine update strategies. Importantly, conventional wild-type mouse models fail to recapitulate strong human SARS-CoV-2 imprinting, which significantly hinders imprinting-related mechanistic investigation and vaccine update evaluation. Here, we surprisingly found that V(D)J-humanized mice could faithfully recapitulate human severe SARS-CoV-2 immune imprinting phenotypes. Comprehensive antibody repertoire and epitope mapping of 583 monoclonal antibodies from these models revealed that the abundance of pre-existing IGHV3-53/66-encoded SARS-CoV-2 antibody responses determines imprinting severity following Omicron exposure through antibody-mediated masking of Omicron-specific epitopes. Both passive transfer of IGHV3-53/66 antibodies and knock-in of the human IGHV3-53 gene were sufficient to induce severe SARS-CoV-2 imprinting in wild-type mice. Concordantly, head-to-head comparison also showed that mRNA vaccine recipients retained higher IGHV3-53/66 antibody abundance and thus stronger imprinting than inactivated vaccine recipients. Consequently, compared to NB.1.8.1, XFG exhibits greater immune evasion in mRNA-vaccinated individuals but not in inactivated vaccine recipients. This explains the regional predominance of XFG in mRNA-vaccinated populations, while NB.1.8.1 prevails in inactivated vaccine-dominated countries. Together, these findings demonstrate that the V(D)J germline repertoire—even a single germline-encoded antibody response—can profoundly shape humoral imprinting severity. Accordingly, we constructed a human IGHV3-53 knock-in mouse model that can accurately recapitulate human SARS-CoV-2 antibody landscape, providing a valuable tool for guiding future COVID-19 vaccine updates.

Main

After extensive global circulation, SARS-CoV-2 continues to co-evolve with human humoral immunity, repeatedly generating variants capable of evading neutralizing antibodies elicited by prior infections and vaccinations [1–11]. Recently, a divergence in SARS-CoV-2 viral circulation has emerged between East and West. In Eastern countries (primarily China), the NB.1.8.1 lineage predominates while XFG remains virtually absent [9]. Conversely, XFG has rapidly risen to dominance in Western regions, leaving NB.1.8.1 as a minor lineage (Extended Data Fig. 1a).

The global deployment of diverse COVID-19 vaccine platforms has consequently established distinct humoral immune landscapes across populations [12–17]. Recipients of mRNA vaccines, primarily in Western countries, exhibit pronounced immune imprinting, persistently recalling ancestral Wuhan-Hu-1 (Wuhan) spike-reactive antibodies even upon repeated Omicron exposures, significantly limiting the development of Omicron-specific neutralizing responses [18–25]. In contrast, individuals only receiving inactivated vaccines, predominantly in China, demonstrate greater adaptability in humoral responses, developing robust Omicron-specific antibodies upon repeated infections or boosters, thus overriding Wuhan immune imprinting [26–29]. These imprinting disparities may potentially contribute to the observed divergence in SARS-CoV-2 epidemiology, raising potential needs for region-specific vaccine update strategies.

The mechanism that drives the divergent SARS-CoV-2 immune imprinting in populations primed with different COVID-19 vaccines is unclear and needs immediate investigation. However, prior studies have shown that, unlike humans, wild-type mice only exhibit weak SARS-CoV-2 ancestral-strain imprinting whether receiving inactivated or mRNA-based vaccine priming [18], limiting the utility of this animal model for both mechanistic investigation of the divergent imprinting and translational vaccine update preclinical research.

In this paper, we present a head-to-head comparison of antibody repertoires, imprinting severity, and responses to emerging variants in individuals primed with mRNA versus inactivated vaccines. These analyses reveal that differences in immune imprinting are already influencing real-world epidemiology, contributing to the distinct regional dominance of XFG and NB.1.8.1. Using V(D)J-humanized mice, we demonstrate faithful recapitulation of strong human-like imprinting and

identify pre-existing IGHV3-53/66-encoded antibodies as the key driver of imprinting severity via epitope masking. Finally, we establish a human IGHV3-53 knock-in mice model that accurately recapitulate human SARS-CoV-2 antibody responses, offering a practical tool for evaluating future vaccine update strategies.

Distinct immune imprinting in humans

To directly compare the humoral immunity in individuals primed with mRNA versus inactivated vaccines, we recruited 20 participants stratified into two cohorts based on vaccination history (Supplementary Table 1 and Fig. 1a). All participants had resided in the same region since 2021 and had experienced multiple Omicron infections. The inactivated-only cohort (n = 12) received three doses of CoronaVac, with samples collected 46.5 ± 5.4 months after the first vaccine dose. The mRNA-vaccinated cohort (n = 8) received at least one mRNA vaccine dose (BNT162b2 or mRNA-1273), with samples collected 46.0 ± 2.3 months after initial vaccination. Although detailed infection histories were unavailable, widespread Omicron transmission following China's reopening strongly suggests that most participants were exposed to at least BA.5 and JN.1 sublineages.

To assess immune imprinting, we first used fluorescence-activated cell sorting (FACS) to quantify cross-reactive memory B cells, defined as the proportion of Wuhan^{+} cells among JN.1^{+} memory B cells (Fig. 1b and Supplementary Information Fig. 1a). The mRNA-vaccinated cohort indeed exhibited a significantly higher proportion of cross-reactive memory B cells than the inactivated-only cohort, indicating stronger imprinting (Fig. 1c). Additionally, the mRNA group showed a higher proportion of Wuhan^{+} memory B cells, reflecting persistent responses to the ancestral strain. In contrast, JN.1^{+} memory B cell frequencies were comparable between groups, suggesting comparable responses to recent variants despite different priming histories (Fig. 1c).

To examine antibody specificity, we depleted Wuhan RBD-binding antibodies from serum and measured the remaining IgG titres against the JN.1 RBD (Fig. 1d). This depletion nearly abolished JN.1-binding activity in the mRNA-vaccinated cohort (19-fold reduction), indicating that the response was almost entirely contributed by cross-reactive antibodies. In contrast, the inactivated-

Figure 1

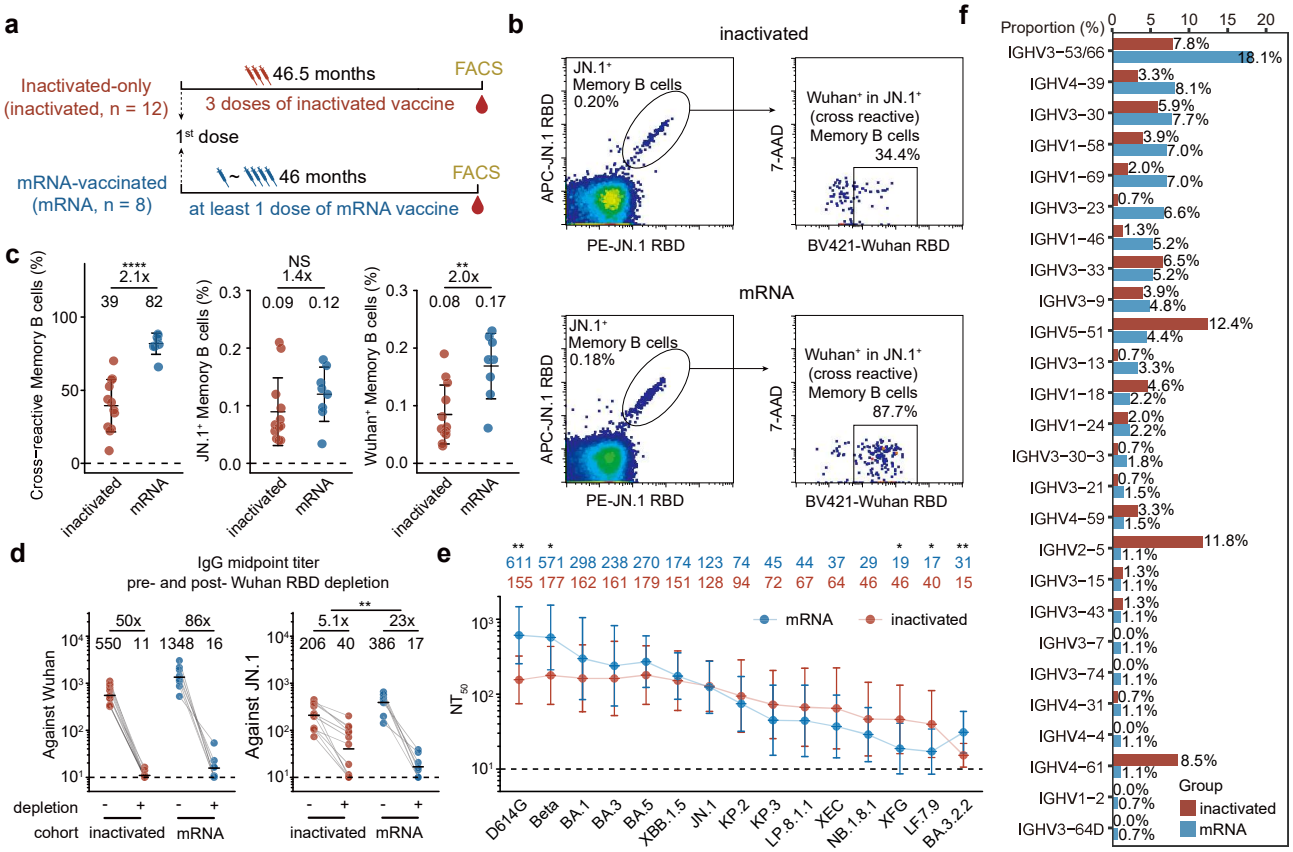

Figure 1 | mRNA and inactivated vaccine priming induce distinct immune imprinting level.
a, Schematic of the SARS-CoV-2-related immune histories and sampling time of the inactivated-only and mRNA-vaccinated cohorts involved in this study. b, Representative flow cytometry dot plots of cross-reactive memory B cells from individuals from the inactivated-only (top) and mRNA-vaccinated (bottom) cohorts. APC, allophycocyanin; PE, phycoerythrin; BV421, Brilliant Violet 421. c, Scatter plots showing the proportion of cross-reactive memory B cells (left), JN.1-reactive memory B cells (middle), and Wuhan-reactive memory B cells (right). d, Serum IgG midpoint titer against Wuhan (left) or JN.1 (right) RBD before and after Wuhan RBD depletion. Statistical significance of the fold-reduction in titers was assessed between two cohorts. Dashed lines indicate the limit of detection (midpoint titre = 10). e, NAb response of the two cohorts against a panel of SARS-CoV-2 variant pseudoviruses. Geometric mean titres (GMTs) are shown on the top. Dashed lines indicate the limit of detection (NT_{50} = 10). f, Heavy chain V gene usage proportion of the two cohorts. IGHV3-53 and IGHV3-66 were combined for analysis. Two-tailed Wilcoxon rank-sum tests were used in c-e. *P < 0.05, **P < 0.01, ***P < 0.001, ****P < 0.0001; NS, not significant (P > 0.05).

103 only cohort showed a more modest decrease (4.4-fold), consistent with the presence of a subset of
104 JN.1-specific antibodies (Fig. 1d).

105 Neutralization assays against a pseudovirus panel further supported this divergence (Fig. 1e). In the
106 mRNA-vaccinated cohort, 50% neutralization titres (NT_{50}) were highest for D614G and declined
107 rapidly with newer variants. In contrast, the inactivated-only cohort maintained relatively stable
108 neutralization, declining only from JN.1 onward. Interestingly, the NT_{50} curves intersected at JN.1,
109 beyond which the inactivated cohort showed higher neutralization. These data suggest that, owing
110 to stronger immune imprinting, the mRNA cohort's neutralizing responses to emerging variants are
111 strongly confined by the recall and expansion of antibodies originally elicited by ancestral exposure,
112 whereas the more adaptable response in the inactivated cohort enables superior neutralization of
113 later-emerging variants.

114 Notably, the mRNA-vaccinated cohort showed a marked reduction in titres against XFG relative to
115 NB.1.8.1, whereas the inactivated-only cohort displayed comparable neutralizing activity against
116 both variants. This disparity provides a serological explanation for the regional predominance of
117 XFG in mRNA-vaccinated populations and NB.1.8.1 in inactivated vaccine-dominated countries [9].
118 Additionally, neutralization titres against BA.3.2 were significantly higher in the mRNA cohort (Fig.
119 1e). This variant carries unique mutations that have been shown to evade Class 1/4 antibodies
120 prevalent in inactivated vaccinees but not the dominant Class 1 antibodies induced by mRNA
121 vaccines [9]. Collectively, these head-to-head comparisons of serological and flow cytometry data
122 confirm robust imprinting in the mRNA-vaccinated cohort and weaker imprinting in the inactivated
123 cohort that can be partially overcome. Such imprinting differences have resulted in distinct antibody
124 landscapes, contributing to regional epidemiological divergence and raising the potential necessity
125 for region-specific vaccine update strategies.

126 While the lack of longitudinal samples makes it challenging to trace the evolutionary mechanism of
127 this divergence in humans, distinct signatures within the BCR repertoire may offer critical insights.
128 To explore these correlates, we performed plate-based single B cell V(D)J sequencing to compare
129 heavy-chain V-gene usage of JN.1^{+} memory B cells between the two cohorts (Fig. 1f) [30]. The
130 mRNA-vaccinated cohort showed enriched usage of IGHV3-53/66—germline genes encoding
131 "public" antibodies targeting the Class 1 epitope, which overlaps with the ACE2-binding site [31–38].

132 These neutralizing antibodies are broadly elicited by Wuhan vaccination or infection and are well
133 known for their potent neutralizing capacity [31,37]. In contrast, the inactivated-only cohort showed
134 greater representation of IGHV5-51 and IGHV2-5, associated with Omicron-specific Class 1/4
135 antibodies [39]. The differences in light chain V-gene usage between the two cohorts were less
136 pronounced, with both groups showing a preference for IGKV1-39, IGKV3-20, and IGKV1-33
137 (Extended Data Fig. 2a).

138 These findings suggest that the IGHV3-53/66–encoded Class 1 antibodies—originally elicited by
139 ancestral Wuhan strain exposure—are preferentially recalled and expanded upon repeated Omicron
140 encounters, and the mRNA-vaccinated cohort exhibits much higher IGHV3-53/66 antibody
141 abundance compared to the inactivated-only cohort, due to its higher priming vaccine
142 immunogenicity. To further dissect the underlying mechanisms and confirm the relationship
143 between immunoglobulin germline genes and severe SARS-CoV-2 imprinting, animal models that
144 faithfully recapitulate these human phenotypes are therefore required.

145

146 **V(D)J-humanized mice mimic strong imprinting**

147 Previous studies have shown that wild-type mice do not recapitulate the strong SARS-CoV-2
148 immune imprinting observed in the human mRNA-vaccinated cohort [18]. Given that our human data
149 identified a critical role for the IGHV3-53/66 germline genes in severe SARS-CoV-2 imprinting,
150 we hypothesized that the absence of these specific human V-genes in the murine repertoire explains
151 this discrepancy. Therefore, we employed V(D)J humanized mice for comparative analysis. These
152 BALB/c-derived mice, commonly used in therapeutic antibody discovery [40], carry human
153 immunoglobulin V(D)J genes for all heavy chains and kappa light chains. Both V(D)J humanized
154 and wild-type mice were primed with three doses of ancestral mRNA vaccine (encoding the spike
155 protein of SARS-CoV-2 ancestral strain), followed by two booster doses of BA.5 mRNA vaccine to
156 mimic human exposure history to SARS-CoV-2 variants (Fig. 2a). Blood, spleens, and lymph nodes
157 were collected one week after the third ancestral dose and each BA.5 dose for serological and flow
158 cytometry analyses.

159 We first performed FACS analysis on mouse lymph nodes to assess cross-reactivity among memory

Figure 2

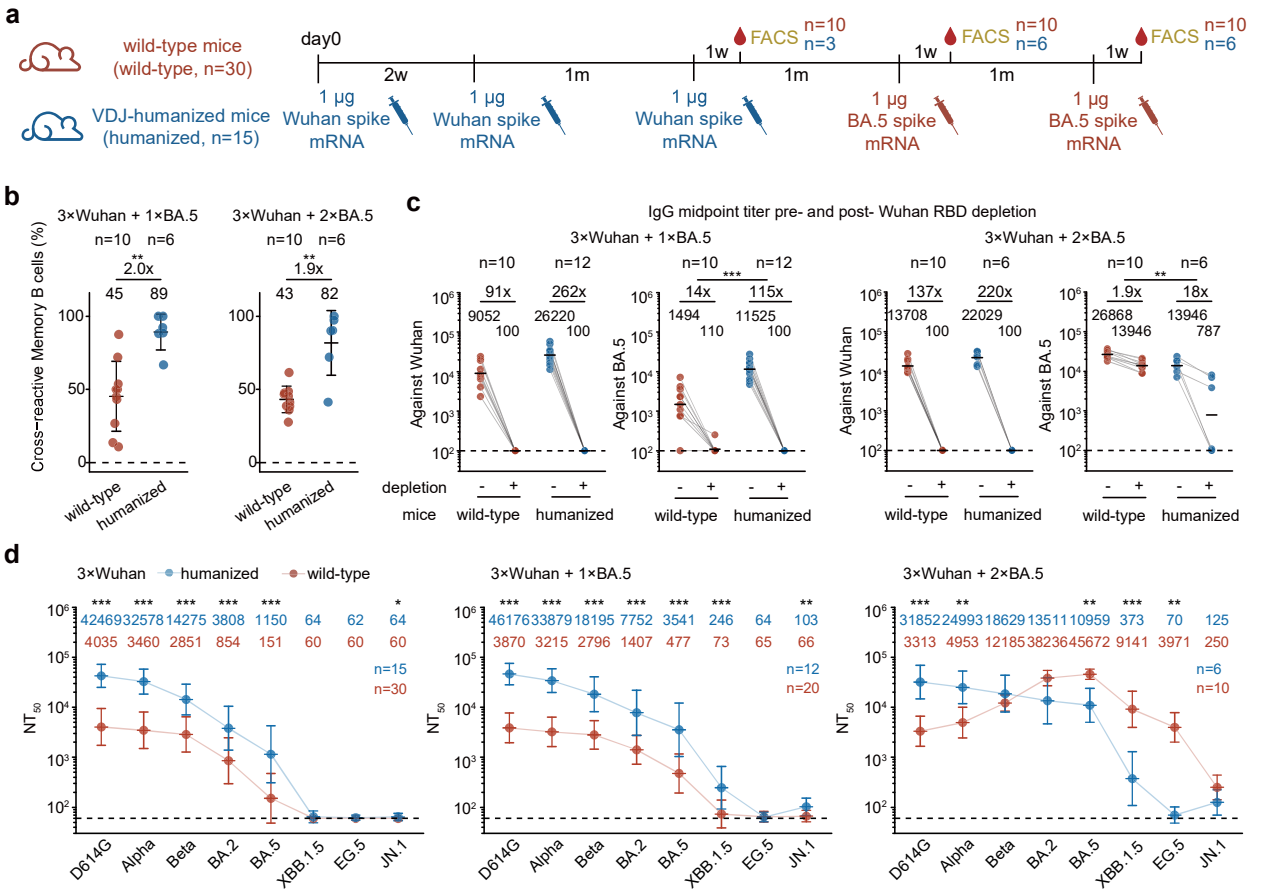

Figure 2 | V(D)J humanized mice recapitulates severe SARS-CoV-2 imprinting.
a, Schematic of the mouse immunization regimen and sampling timeline for wild-type and V(D)J-humanized mice. The number of mice is indicated at the time point for each endpoint experiment. b, Scatter plots showing the proportion of cross-reactive memory B cells in draining lymph nodes of the two mouse strains after one (left) or two (right) BA.5 boosts. c, Serum IgG midpoint titer of the two mouse strains after one (left) or two (right) BA.5 boosts against Wuhan or BA.5 RBD before and after Wuhan RBD depletion. Statistical significance of the fold-reduction in titers was assessed between humanized and wild-type mice. Dashed lines indicate the limit of detection (midpoint titre = 100). d, Serum neutralization titers (NT_{50}) of the two mouse models after Wuhan priming (left), one BA.5 boost (middle), or two BA.5 boosts (right) against a panel of SARS-CoV-2 variant pseudoviruses. Geometric mean titres (GMTs) are shown on the top. Dashed lines indicate the limit of detection (NT_{50} = 60). Two-tailed Wilcoxon rank-sum tests were used in b-d.

160 B cells and germinal-center (GC) B cells (Supplementary Information Fig. 1b). As expected, wild-
161 type mice harbored abundant BA.5-specific memory and GC B cells after each BA.5 booster (Fig.
162 2b and Extended Data Fig. 3a). In striking contrast, the V(D)J-humanized mice exhibited a strong
163 imprinting phenotype, developing a high proportion of cross-reactive memory B cells (89% and 82%
164 after the first and second boosters, respectively) that mirrored the response observed in the human
165 mRNA cohort. Despite similar overall percentages of GC B cells, humanized mice showed a
166 significantly higher frequency of cross-reactive GC B cells after one BA.5 booster, indicating that
167 their GC response was dominated by Wuhan-strain imprinted B cells (Extended Data Fig. 3a and
168 3b). Additionally, they presented a significantly higher frequency of class-switched memory B cells,
169 which aligns with the preferential recall and expansion of a pre-existing memory population typical
170 of immune imprinting (Extended Data Fig. 3c).

171 The imprinting was also faithfully reflected in the serological response. Wuhan RBD-depletion
172 caused a substantially greater drop in BA.5-binding IgG titres in humanized mice than in wild-type
173 mice (10-fold vs. 2.1-fold), although the magnitude of this effect varied among individual
174 humanized mice (Fig. 2c). Specifically, titres in three humanized mice dropped to undetectable
175 levels, while the remaining three exhibited modest reductions. The post-depletion titre ratio was
176 inversely correlated with the proportion of cross-reactive memory B cells (Extended Data Fig. 3d),
177 demonstrating consistency between cellular and serological assays and reflecting individual
178 heterogeneity in imprinting strength.

179 We next compared serum neutralization profiles between the two mouse models (Fig. 2d and
180 Extended Data Fig. 4a). Initially, following Wuhan priming, humanized mice mounted a
181 significantly more potent and broad response than wild-type mice. Two BA.5 boosters successfully
182 shifted the NAb preferences of wild-type mice toward Omicron variants. In contrast, the
183 neutralization curves of humanized mice closely mirrored those of the mRNA cohort, with titres
184 remaining maximal against D614G despite repeated Omicron exposure, indicating strong immune
185 imprinting that could not be overcome by two doses of BA.5 boosting. (Extended Data Fig. 4a).
186 Together, these data collectively demonstrate that humanized mice can mirror SARS-CoV-2
187 imprinting. This divergence between the two mouse models strongly suggests that the presence of
188 human immunoglobulin V(D)J genes is a critical determinant of the imprinting phenotype.

189

190 **Distinct antibody landscapes of mouse models**

191 To dissect the molecular basis of imprinting, we interrogated the evolution of antibody repertoire
192 from the two mouse models at single-B-cell resolution. We sorted RBD-specific memory B cells
193 from spleens of humanized and wild-type mice following Wuhan priming (sorted on Wuhan RBD)
194 and after each BA.5 booster (sorted on BA.5 RBD; Supplementary Information Fig. 1c). Single-cell
195 V(D)J sequencing of paired heavy- and light-chain variable regions generated 583 unique
196 monoclonal antibodies from the six mice groups, which were recombinantly expressed as human
197 IgG1 (Supplementary Table 2). Consistent with the established imprinting signature, antibodies
198 from humanized mice showed a higher proportion of cross-reactivity than those from wild-type
199 mice (Extended Data Fig. 5a and 5b).

200 To systematically dissect the divergence in antibody epitope distribution between humanized and
201 wild-type mice, we employed high-throughput yeast-display-based deep mutational scanning (DMS)
202 to map the RBD mutations that could escape the isolated mAbs and define the epitope targeted
203 [28,41,42]. We built single-site saturation mutant libraries based on the Wuhan-Hu-1 and BA.5 RBDs
204 and performed DMS for antibodies isolated following Wuhan priming or BA.5 boosting,
205 respectively. The resulting escape profiles of 583 monoclonal antibodies define the critical residues
206 that mediate immune evasion and facilitating their precise categorization into distinct epitope
207 clusters.

208 IC50-weighted escape profiles show that neutralizing antibodies from wild-type and humanized
209 mice exhibit distinct escape hotspot sites (Fig. 3a-3c and Extended Data Fig. 6a-6c). Following
210 Wuhan priming, the NAbs elicited in humanized mice substantially focused on Class 1 epitopes,
211 featured by hotspots at residues 417, 456, 460, and 473. Although wild-type mice displayed a
212 comparable landscape after Wuhan priming, they lacked these Class 1 peaks, instead featuring
213 residue 477 as a characteristic hotspot (Fig. 3a). BA.5 boosting leads to further divergence
214 between the two mouse models. In humanized mice, the prominent Class 1 hotspots (e.g., residue
215 456) persisted obstinately throughout the boosting regimen. In contrast, the wild-type repertoire
216 diverged significantly upon boosting, characterized by the emergence of distinct Class 1/4 escape

Figure 3

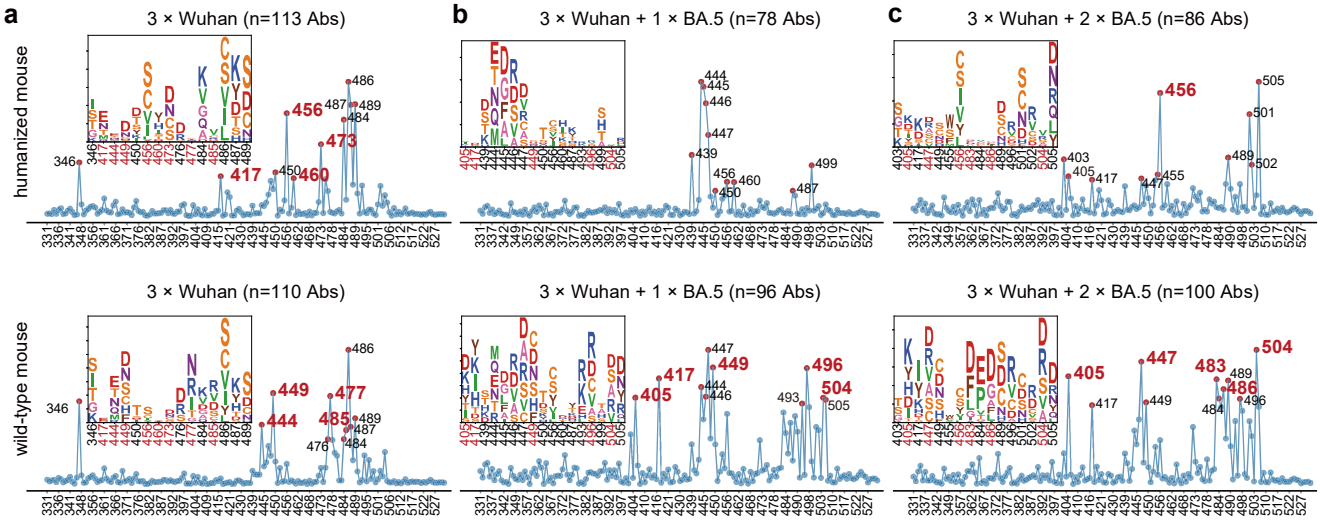

Figure 3 | Distinct antibody landscapes between mRNA vaccinated humanized and wild-type mice.
a–c, Normalized average DMS escape scores for mAbs isolated from humanized (top) and wild-type (bottom) mice following Wuhan priming (a), the first BA.5 booster (b), or the second BA.5 booster (c). Escape scores were aggregated and weighted by the IC_{50} of each individual mAb (To focus on the neutralizing mAbs, lower IC_{50} corresponds to greater weight) against D614G for Wuhan-primed groups or BA.5 for BA.5-boosted groups. Codon constraints were applied (see Methods). In each panel, the ten residues with the highest cumulative escape scores are annotated, with their specific mutational escape profiles visualized as logo plots above the scatter plots. To highlight divergent immune pressure, residues exhibiting pronounced differences between humanized and wild-type strains (as identified in Extended Data Fig. 6) are colored red in both the scatter plots and logo plots.

217 peaks, such as residue 504 (Fig. 3b-3c).

218 To translate these differences in escape sites into a more intuitive view of epitope-level repertoire
219 differences, we categorized the 583 mAbs into 9 epitope groups (Supplementary Information Fig.
220 2a) [28]. Names of the epitope groups were generally assigned in line with the epitope groups on
221 Wuhan RBD defined previously [43,44]. We then comprehensively analyzed the antibody repertoires
222 elicited in humanized and wild-type mice after each timepoint (Fig. 4a and 4b, Extended Data Fig.
223 7a-7d). Following Wuhan priming, humanized mice uniquely elicited a dominant population of
224 antibodies targeting the A1 epitope (Fig. 4a). Notably, antibodies targeting this epitope are closely
225 related to the IGHV3-53 germline and target key residues such as 456, aligning with the escape
226 hotspots. The foundational divergence between the two mouse models was established immediately
227 after Wuhan priming. After two BA.5 boosting doses, while dynamic shifts occurred—including the
228 abrogation of Group B and the emergence of Group A2—the A1 response remained persistent in
229 humanized mice (Fig. 4c and Extended Data Fig. 7a and 7c). In contrast, Omicron-specific
230 antibodies in epitope groups B, D, and F3 contribute mostly to the neutralization against BA.5
231 exclusively in wild-type but not the V(D)J-humanized mice.

232 Overall, DMS analysis demonstrates that Class 1 (A1) antibodies play a pivotal role in the response
233 to Wuhan priming, serving as a defining characteristic of the V(D)J-humanized mouse model,
234 compared to the wild-type mice. This antibody subset substantially contributed to the polyclonal
235 neutralization landscape and could be robustly recalled upon BA.5 boosting. Notably, these A1
236 antibodies exhibited remarkable germline convergence, consistently dominated by IGHV3-53 after
237 both Wuhan priming and subsequent BA.5 boosting (Fig. 4a). This mirrors the IGHV3-53/3-66
238 dominance observed in mRNA-vaccinated human cohorts. Collectively, these findings led us to
239 hypothesize that the dominant, IGHV3-53/66-driven A1 antibody response induced by Wuhan
240 priming is the mechanistic driver of SARS-CoV-2 immune imprinting.

241

242 **Molecular mechanism of imprinting**

243 Given that immune imprinting relies on the recall of pre-existing memory B cells, we then confirmed
244 the cross-reactivity of these IGHV3-53/66-encoded A1 antibodies to determine their potential for

Figure 4

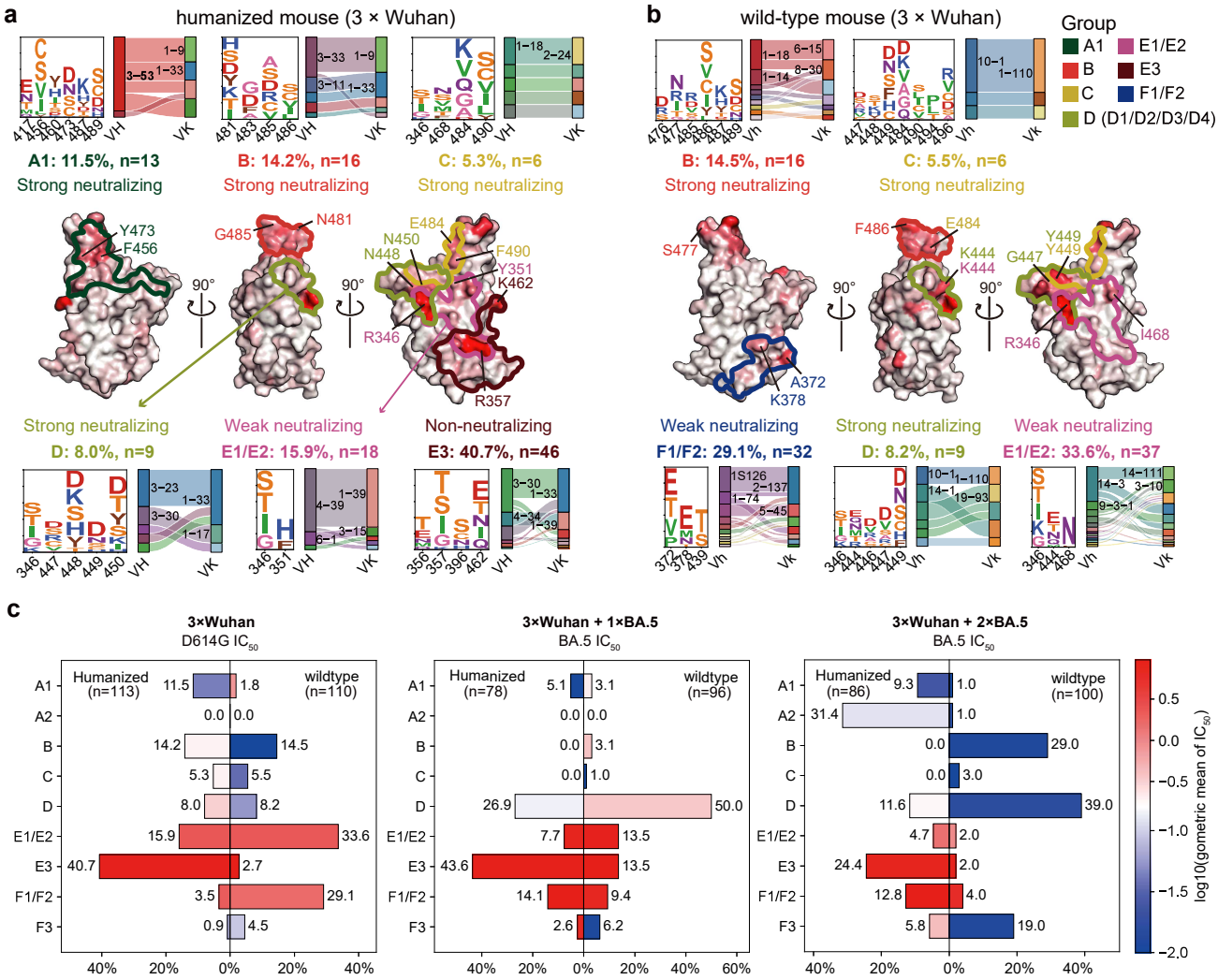

Figure 4 | VDJ germline difference shapes vaccination- induced SARS-CoV-2 antibody epitope distribution.
Epitope distribution of the antibody repertoire generated after Wuhan priming in humanized (a) and wild-type mice (b). The Wuhan RBD structure (PDB: 6m0j) is displayed as a surface map colored by normalized aggregate escape scores, with epitope groups outlined in distinct colors. Their neutralizing category (Strong, Weak, or Non-neutralizing), antibody count, and percentage are indicated. Key escape residues for each group are displayed as logos, and the sites with the highest escape scores per group are labeled on the structure. Paired heavy and light chain V-gene usage for each epitope is shown in Sankey plots. c, Pyramidal bar charts showing the proportional distribution of epitope groups in antibodies isolated from humanized and wild-type mice after Wuhan priming and after one or two BA.5 boosts. Bars are colored according to the log10 geometric mean IC_{50} of antibodies within each group.

245 reactivation by the Omicron booster (Fig. 5a). 38% of A1 mAbs from Wuhan-primed humanized
246 mice were cross-reactive, constituting a pre-existing memory pool that was efficiently recalled to
247 achieve 100% cross-reactivity upon BA.5 boosting. In contrast, the negligible A1 response in
248 primed wild-type mice was entirely Wuhan-specific, making subsequent boosters elicited only rare,
249 *de novo* BA.5-specific A1 antibodies. Competitive SPR mapping revealed that A1 antibodies
250 compete with ACE2 and the majority of antibodies targeting neutralizing epitopes (A2, B, C, D4,
251 F3). Conversely, they showed minimal to no competition with Group D1 or the weakly or non-
252 neutralizing E and F antibodies (Fig. 5b).

253 These results indicate that A1 antibodies can sterically mask most other major neutralizing sites on
254 Omicron RBD from access by other antibodies and their corresponding B cell receptors. Enabled
255 by the IGHV3-53/66 germline genes, Wuhan priming induces a high-frequency pool of these potent
256 "masking" antibodies, the abundance of which scales directly with the intensity of the priming.
257 Critically, a significant portion of this pool is not escaped by Omicron and remains cross-reactive,
258 making it available for recall upon subsequent Omicron exposure. Therefore, during Omicron
259 vaccination, this pre-existing and cross-reactive memory B cell population is preferentially
260 reactivated and expanded. This potent, recalled response actively outcompetes and suppresses the
261 *de novo* activation of B cells targeting novel, Omicron-specific epitopes by masking, providing a
262 direct mechanistic basis for the strong immune imprinting observed in humanized mice. (Fig. 5c).

263 To test whether these antibodies can indeed drive strong imprinting *in vivo*, we performed passive
264 antibody transfer experiments in wild-type mice (Fig. 5d). Wuhan-primed wild-type mice were
265 infused with BD55-1205 (a representative IGHV3-66-encoded A1 broad neutralizing antibody [45])
266 at various doses and formats (human or mouse IgG1) one day prior to BA.5 boosting (Fig. 5d-5e).
267 Controls received either PBS or a non-neutralizing antibody (BD57-2665, a representative F1
268 antibody targeting the cryptic sites of RBD, Fig. 5e). Flow cytometry analysis of lymph nodes
269 showed that mice receiving 400 μg or 200 μg BD55-1205 hIgG1 and 200 μg BD55-1205 mIgG1
270 developed pronounced imprinting, evidenced by significantly elevated frequencies of cross-reactive
271 memory B cells at both post-boost time points compared with PBS controls (Fig. 5f). After the first
272 BA.5 boost, GC B cells in BD55-1205–treated mice also showed markedly higher cross-reactivity,
273 demonstrating that early maturation and clonal expansion within the GC was dominated by recalled,

Figure 5

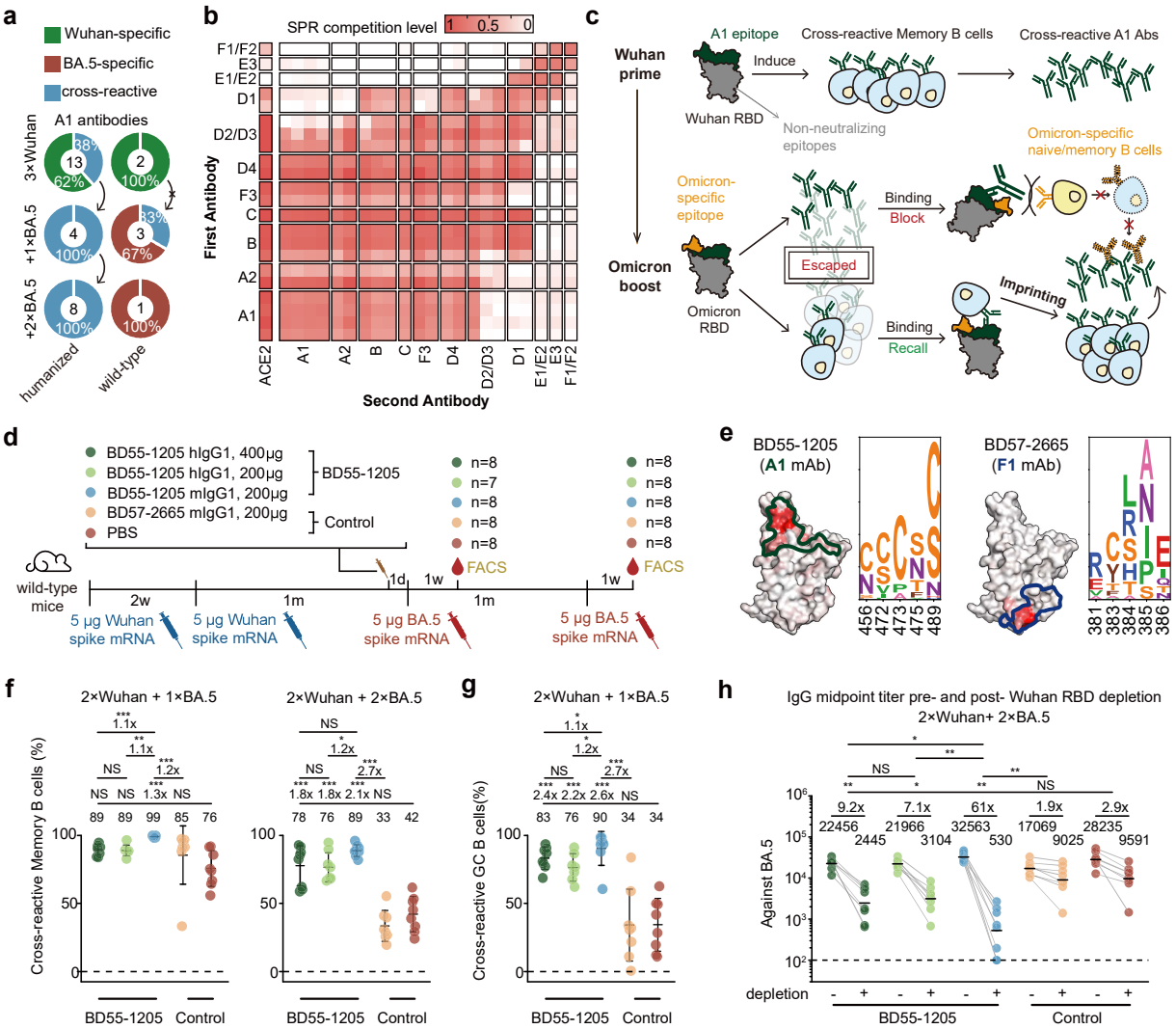

Figure 5 | IGHV3-53/66-encoded Class 1 antibody drives SARS-CoV-2 imprinting through epitope masking.
a, Donut plots showing the cross-reactivity of A1 antibodies from humanized or wild-type mice. The number of antibodies are indicated in the centre of the donut. b, Heatmap of competitive SPR for various antibody groups. The definition of the competition score is described in the Methods section. c, Schematic of the molecular mechanism by which pre-existing IGHV3-53/66-encoded A1 antibodies cause strong immune imprinting. d, Schematic of the antibody passive transfer experiment. Timing of mRNA vaccinations, antibody injection, blood collection, and FACS analysis are indicated. Mice were divided into experimental groups (receiving 400 μg BD55-1205 hIgG1, 200 μg BD55-1205 hIgG1, or 200 μg BD55-1205 mIgG1) and control groups (receiving 200 μg BD57-2665 mIgG1 or PBS). The number of mice per group is indicated at the endpoint. e, DMS escape map logoplots for BD55-1205 and BD57-2665 and their projection onto the SARS-CoV-2 Wuhan RBD (PDB: 6m0j). f, Scatter plots showing the proportion of cross-reactive memory B cells in draining lymph nodes after one (left) or two (right) BA.5 boosts. g, Scatter plots showing the proportion of cross-reactive germinal center B cells in draining lymph nodes after one BA.5 boost. h, Serum IgG midpoint titer against BA.5 RBD before and after Wuhan RBD depletion. Statistical significance of the fold-reduction in titers was assessed between groups. Dashed lines indicate the limit of detection (midpoint titre = 100). Two-tailed Wilcoxon rank-sum tests were used in f-h.

274 imprint-driven B cells (Fig. 5g). In contrast, BD57-2665 mIgG1–treated mice showed no significant
275 change in cross-reactive memory B cell or GC B cell frequencies, indicating that non-neutralizing
276 antibody blockade does not induce imprinting, ruling out the possibility that the transferred antibody
277 simply depleted the vaccine antigen and prevented a successful BA.5 immunization (Fig. 5f-5g).
278 Correspondingly, Wuhan-RBD depletion of serum from BD55-1205–treated mice produced a more
279 severe drop in BA.5 IgG titres, whereas BD57-2665 mIgG1 and PBS groups showed minimal titre
280 reduction (Fig. 5h). Notably, the mIgG1 format induced a significantly stronger imprinting
281 phenotype than hIgG1, which is likely attributable to the species-matched Fc region (Fig. 5f-5h).
282 Pharmacokinetic analysis confirmed that the passively transferred antibodies had decayed to near-
283 undetectable levels by the time of analysis, thus eliminating their potential interference with ELISA
284 measurements (Extended Data Fig. 8a-8b). Importantly, we demonstrated that the suppressive effect
285 of BD55-1205 on the BA.5-specific response was dose-dependent, with doses as low as 12.5 μg
286 being sufficient to achieve inhibition (Extended Data Fig. 8c-8d). Together, these results confirm
287 that IGHV3-53/66-encoded A1 neutralizing antibodies not only compete with other neutralizing
288 antibodies *in vitro* but also suppress the emergence of Omicron-specific B cell and antibody
289 responses to induce severe imprinting *in vivo*.

290 This explains why immune imprinting is recapitulated in V(D)J-humanized mice but not in wild-
291 type mice—only the former harbor this human germline gene required to produce such imprinting-
292 prone antibodies. Similarly, in mRNA-vaccinated individuals, the potent Wuhan priming response
293 by mRNA vaccination (elicited by monovalent Wuhan vaccines and, in certain populations, bivalent
294 Wuhan/BA.1 or Wuhan/BA.5 vaccines) induces a larger pool of IGHV3-53/66-encoded A1
295 antibodies, thereby establishing pronounced imprinting. In contrast, recipients of inactivated
296 vaccines typically experience weaker priming responses and, following stringent containment
297 policies during 2021-2022, undergo substantial waning of Wuhan antibodies. This attenuated pre-
298 existing immunity, leading to lower IGHV3-53/66 antibody abundance, fails to fully suppress
299 subsequent Omicron-specific responses, resulting in more flexible and adaptive humoral evolution.

300

301 **IGHV3-53 knock-in mouse model**

302 Since wildtype mice could not recapitulate human SARS-CoV-2 immune imprinting observed in
303 mRNA vaccine recipients, evaluating SARS-CoV-2 vaccine updates and broad-spectrum vaccine
304 design in mice is highly problematic. Although V(D)J-humanized mice could capture human
305 imprinting phenotypes, its significant cost creates a pressing need for a more accessible and cost-
306 effective model for vaccine evaluation. Building on our finding that the human IGHV3-53/66
307 germline is the primary driver of immune imprinting, we engineered a knock-in mouse model by
308 replacing the murine Ighv3-1 gene with human IGHV3-53. This generated both heterozygous
309 (IGHV3-53$^{+/-}$) and homozygous (IGHV3-53$^{+/+}$) mice. High-throughput Genome-wide
310 Translocation Sequencing (HTGTS) of the naïve B cell repertoire confirmed the successful knock-
311 in, revealing IGHV3-53 usage at 0.5% in homozygous and 1.5% in heterozygous mice, with a
312 corresponding ablation of IGHV3-1 usage (0.1% and 0.0%, respectively, Fig. 6a).

313 To test the model, we immunized wild-type, heterozygous, and homozygous mice using the same
314 regimen of three Wuhan primes followed by two BA.5 boosts (Fig. 6b). Subsequent flow cytometry
315 analysis and depletion assays confirmed that both IGHV3-53$^{+/-}$ and IGHV3-53$^{+/+}$ mice faithfully
316 recapitulated the strong immune imprinting phenotype (Fig. 6c-6d). The serum neutralization
317 profiles of IGHV3-53$^{+/-}$ and IGHV3-53$^{+/+}$ mice also showed a trend remarkably similar to that of
318 the V(D)J-humanized mice (Fig. 6e and Extended Data Fig. 9a). These results demonstrate that both
319 heterozygous and homozygous IGHV3-53 knock-in mice faithfully recapitulate the strong immune
320 imprinting phenotype.

321 We subsequently utilized this model to simulate the real-world SARS-CoV-2 exposure history
322 characteristic of mRNA-vaccinated populations (Fig. 6f). Specifically, mice received a two-dose
323 Wuhan priming series, mimicking the standard primary course. This was followed by sequential
324 boosters with bivalent Wuhan/BA.1 and Wuhan/BA.5 vaccines, a monovalent XBB.1.5 vaccine,
325 and a monovalent JN.1 vaccine, corresponding to the recommended mRNA booster updates during
326 the Omicron era. These regimens effectively reconstruct the antigenic trajectory of SARS-CoV-2
327 evolution encountered by humans. Compared to wild-type controls, IGHV3-53$^{+/+}$ mice recapitulated
328 a more pronounced immune imprinting phenotype following the six-dose regimen. Specifically,
329 while retaining potent neutralization against D614G and early Omicron variants (antecedent to JN.1,
330 Fig. 6g), IGHV3-53$^{+/+}$ mice exhibited a compromised breadth of neutralization against the newly

Figure 6

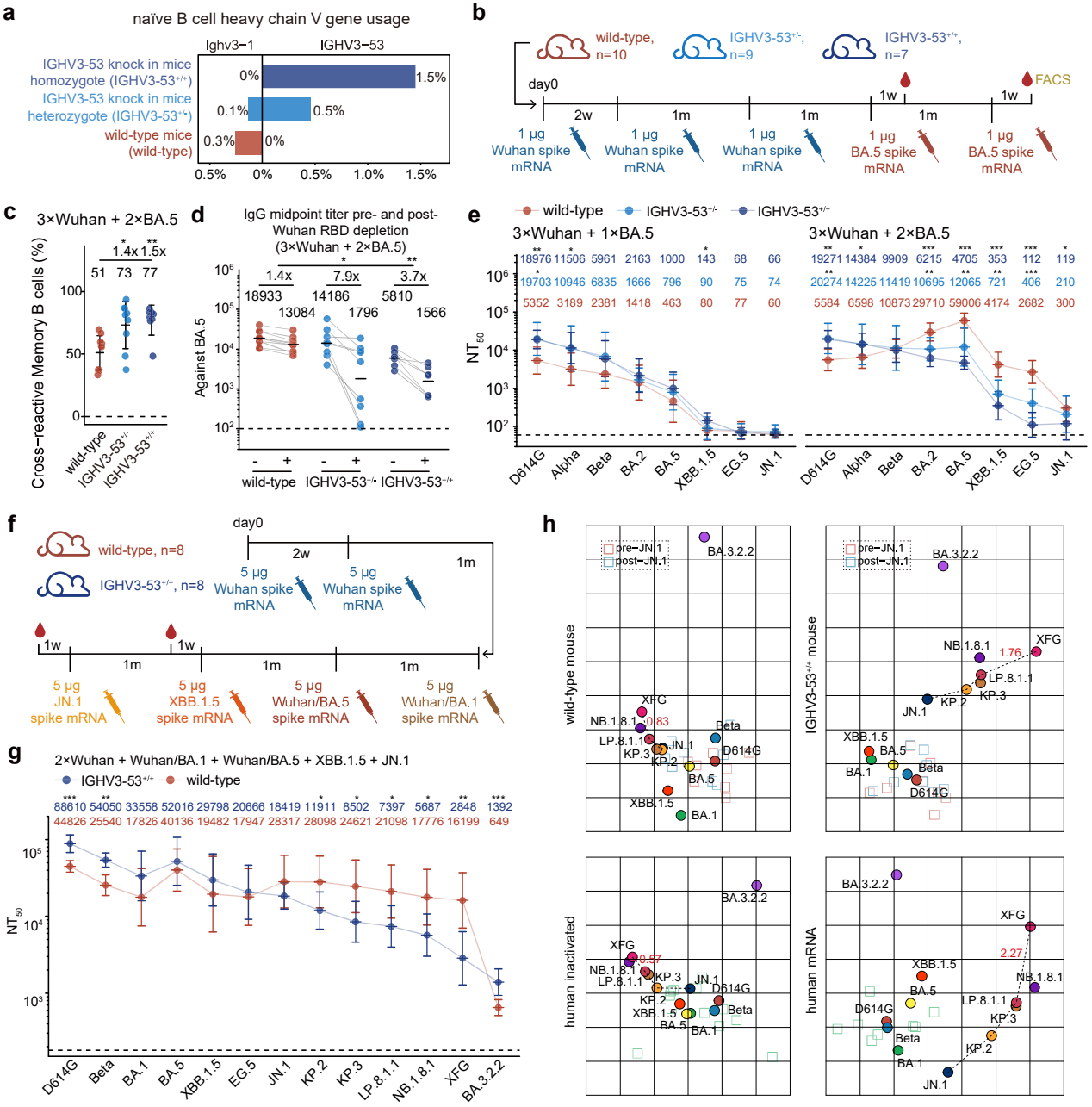

Figure 6 | IGHV3-53 knock-in mouse faithfully reflects SARS-CoV-2 antibody map in human.
a, Usage percentage of IGHV3-53 and Ighv3-1 in naïve B cells from HTGTS sequencing of IGHV3-53$^{+/+}$ (balb/c), IGHV3-53$^{+/-}$ (balb/c* C57B6/J), and wild-type (C57B6/J) mice. b, Schematic of the immunization regimen and time points for blood collection and FACS analysis of the three mouse models involved in this study. The number of mice is indicated above the timeline. c, Scatter plots showing the proportion of cross-reactive memory B cells in draining lymph nodes of the three mouse models after two BA.5 boosts. d, Serum IgG midpoint titer of the three mouse strains after two BA.5 boosts against BA.5 RBD before and after Wuhan RBD depletion. Statistical significance of the fold-reduction in titers was assessed between groups. Dashed lines indicate the limit of detection (midpoint titre = 100). e, Serum neutralization titers (NT_{50}) of the three mouse strains after one (left) or two (right) BA.5 boosts against a panel of SARS-CoV-2 variant pseudoviruses. Geometric mean titres (GMTs) are shown on the top. Dashed lines indicate the limit of detection (NT50 = 60). f, Schematic of the immunization regimen simulating real-world SARS-CoV-2 exposure history. g, Serum neutralization titers (NT_{50}) of IGHV3-53$^{+/+}$ and wild-type mice against a panel of SARS-CoV-2 variant pseudoviruses. Geometric mean titres (GMTs) are shown on the top. Dashed lines indicate the limit of detection (NT_{50} = 180). h, Antigenic cartography was performed using mouse (top) and human (bottom) plasma neutralization data. Each square indicates a plasma sample, and each circle indicates a SARS-CoV-2 variant. Two-tailed Wilcoxon rank-sum tests were used in c-e and g.

331 emerged JN.1 sublineages. Specifically, titers against KP.2, KP.3, LP.8.1.1, NB.1.8.1, and XFG were
332 significantly suppressed compared to those in wild-type mice, indicating an inhibition of de novo
333 responses to the newly emerged Omicron-specific epitopes in these variants. (Fig. 6g). Notably,
334 IGHV3-53$^{+/+}$ mice showed higher neutralization titres against BA.3.2 than wild-type mice (Fig. 6g),
335 mirroring the specific serological feature observed in the human mRNA cohort (Fig. 1e). Similar
336 trends were observed after five doses (Extended Data Fig. 10a). Furthermore, comparing
337 neutralization profiles pre- and post-JN.1 boost revealed a strong back-boosting effect in IGHV3-
338 53$^{+/+}$ mice, where JN.1 immunization significantly elevated titres against antecedent strains (pre-
339 JN.1). In contrast, wild-type mice displayed no such effect and even exhibited a significant decline
340 in D614G titres (Extended Data Fig. 10b).

341 Consequently, the two mouse models exhibited distinct susceptibility to viral escape. Following
342 XBB.1.5 immunization, neutralization against EG.5 was significantly reduced compared to
343 XBB.1.5 in IGHV3-53$^{+/+}$ mice, a reduction not seen in wild-type mice (Extended Data Fig. 10c).
344 Similarly, after the JN.1 boost, IGHV3-53$^{+/+}$ mice showed significant susceptibility to escape by
345 KP.2 and KP.3 relative to JN.1, whereas wild-type mice did not. Consistently, the fold-reduction in
346 titres against XFG relative to NB.1.8.1 was greater in IGHV3-53$^{+/+}$ mice than in wild-type mice
347 (Extended Data Fig. 10c). This result faithfully recapitulates the serological divergence observed
348 between the human mRNA-vaccinated and inactivated-only cohorts (Fig. 1e), and matches the
349 variant escaping profiles of V3-53/66 Class 1 NAbs. By leveraging the genetic precision of the
350 IGHV3-53 knock-in model to eliminate confounding immune histories, we definitively confirm that
351 the imprinted, V3-53/66-dominated response inherently renders mRNA recipients more susceptible
352 to immune evasion by such emerging variants

353 To visualize how IGHV3-53$^{+/+}$ mice could help with SARS-CoV-2 vaccine update evaluation, we
354 constructed antigenic cartography using serum neutralization data from both mouse models and
355 human cohorts (Fig. 6h). The resulting maps revealed striking topological differences. Wild-type
356 mice exhibited a 'condensed' antigenic landscape similar to the inactivated-only cohort,
357 characterized by short antigenic distances between all JN.1 sublineages. In contrast, the antigenic
358 map of IGHV3-53$^{+/+}$ mice closely mirrors that of mRNA-vaccinated cohort, with both displaying
359 substantial antigenic distances between JN.1, KP.2, KP.3/LP.8.1.1, and XFG, supporting vaccine

antigen updates. Crucially, only the IGHV3-53$^{+/+}$ model faithfully reproduces the substantial antigenic distance (~2) between XFG and LP.8.1.1 characteristic of the mRNA cohort. These findings further implicate the IGHV3-53 knock-in mice could faithfully recapitulates human SARS-CoV-2 immune imprinting, and can serve as a superior model for preclinical SARS-CoV-2 vaccine evaluation.

Discussion

Overall, our study establishes that the abundance of pre-existing IGHV3-53/66-encoded Class 1 antibodies is the primary determinant of SARS-CoV-2 immune imprinting severity. Specifically, three converging factors—the inherent potent immunogenicity of mRNA platforms in human [46], the widespread administration of bivalent mRNA boosters containing Wuhan components in Western populations, and the substantial antibody waning in inactivated vaccine recipients due to strict containment policies (e.g., zero-COVID in China) [47–49]—sufficiently infer that mRNA vaccinees harbored a significantly higher abundance of IGHV3-53/66-encoded Class 1 antibodies prior to their Omicron exposure. Consequently, this mRNA-vaccinated population exhibits a more robust humoral imprinting phenotype. As these distinct humoral immune landscapes became established, a parallel divergence in viral evolution emerged, characterized by the regional predominance of XFG and NB.1.8.1. This co-evolution highlights the necessity of incorporating regional immunological differences into vaccine update strategies.

Importantly, we developed an accessible and robust IGHV3-53 knock-in mouse model that overcomes the limitations of wild-type mice, which fail to recapitulate the SARS-CoV-2 imprinting phenotype. By simulating real-world SARS-CoV-2 exposure histories in this model, we successfully mapped the humoral response landscape of mRNA human vaccinees in mice. Moving forward, this model should be leveraged to conduct parallel evaluations of boosting regimens derived from diverse, newly emerging variants. Such comparative studies will provide the essential data support required to guide the further updating and optimization of SARS-CoV-2 vaccines. Furthermore, as a platform that explicitly exposes the 'imprinted barrier' of mRNA recipients, it would enable the future research of vaccine candidates capable of overcoming such entrenched imprinting.

Data and code availability

Information of individuals providing blood samples and isolated mAbs involved in this study have been included in the Supplementary Tables. All data and materials presented in this manuscript are available from the lead contact upon a reasonable request under a completed Material Transfer Agreement. Further information and requests for resources and reagents should be directed to and will be fulfilled by the lead contact, yunlongcao@pku.edu.cn (Y.C.).

Acknowledgments

We thank all volunteers who provided blood samples. This project is financially supported by the Ministry of Science and Technology of China (2022ZD0115002, Y.C.) and Changping Laboratory (2025D-04-01 to Y.C.).

Author contributions

Y.C. designed and supervised the study. X.N., F.J. and Y.C. wrote the manuscript with input from all authors. X.N., W.S., R.A. and Y.W. performed B cell sorting, single-cell V(D)J sequencing experiments and data analysis. X.N., Y.L., K.L., S.L., R.K., X.C., R.A., and Y.W. performed FACS analysis. H.S. and F.J. obtained and analyzed the DMS data. J.W. and F.S. performed antibody expression. W.W. constructed mRNA vaccines and conducted mouse immunization. Y.Y. constructed the pseudotyped virus. L.Y. performed the pseudovirus neutralization assays, ELISAs and SPR experiments. Y.H., S.L., X.N. and Y.L. performed the HTGTS-Rep-seq and data analysis. B.Z., T.Z., J.H., and X.T. recruited the patients and collected the blood samples.

Declaration of interests

Provisional patents related to the antibodies mentioned in this paper have been filed. Y.C. is a co-founder of Singlomics Biopharmaceuticals. Other authors declare no competing interests.

References

1. Addetia, A. *et al.* Neutralization, effector function and immune imprinting of Omicron

variants. *Nature* **621**, 592–601 (2023).
2. Raharinirina, N. A. *et al.* SARS-CoV-2 evolution on a dynamic immune landscape. *Nature* **639**, 196–204 (2025).
3. Mellis, I. A. *et al.* Antibody evasion and receptor binding of SARS-CoV-2 LP.8.1.1, NB.1.8.1, XFG, and related subvariants. 2025.07.18.662329 Preprint at https://doi.org/10.1101/2025.07.18.662329 (2025).
4. Carabelli, A. M. *et al.* SARS-CoV-2 variant biology: immune escape, transmission and fitness. *Nat. Rev. Microbiol.* **21**, 162–177 (2023).
5. Yuan, M. & Wilson, I. A. Structural Immunology of SARS-CoV-2. *Immunol. Rev.* **329**, e13431 (2025).
6. Holmes, E. C. The Emergence and Evolution of SARS-CoV-2. *Annu. Rev. Virol.* **11**, 21–42 (2024).
7. Telenti, A., Hodcroft, E. B. & Robertson, D. L. The Evolution and Biology of SARS-CoV-2 Variants. *Cold Spring Harb. Perspect. Med.* **12**, a041390 (2022).
8. Markov, P. V. *et al.* The evolution of SARS-CoV-2. *Nat. Rev. Microbiol.* **21**, 361–379 (2023).
9. Guo, C. *et al.* Antigenic and virological characteristics of SARS-CoV-2 variants BA.3.2, XFG, and NB.1.8.1. *Lancet Infect. Dis.* **25**, e374–e377 (2025).
10. Liu, J. *et al.* Enhanced immune evasion of SARS-CoV-2 variants KP.3.1.1 and XEC through N-terminal domain mutations. *Lancet Infect. Dis.* **25**, e6–e7 (2025).
11. Liu, J. *et al.* Virological and antigenic characteristics of SARS-CoV-2 variants LF.7.2.1, NP.1, and LP.8.1. *Lancet Infect. Dis.* **25**, e128–e130 (2025).
12. García-Montero, C. *et al.* An Updated Review of SARS-CoV-2 Vaccines and the Importance of Effective Vaccination Programs in Pandemic Times. *Vaccines* **9**, 433 (2021).
13. Yang, Z.-R. *et al.* Efficacy of SARS-CoV-2 vaccines and the dose–response relationship with three major antibodies: a systematic review and meta-analysis of randomised controlled trials. *Lancet Microbe* **4**, e236–e246 (2023).
14. Creech, C. B., Walker, S. C. & Samuels, R. J. SARS-CoV-2 Vaccines. *JAMA* **325**, 1318–1320 (2021).
15. Kyriakidis, N. C., López-Cortés, A., González, E. V., Grimaldos, A. B. & Prado, E. O. SARS-CoV-2 vaccines strategies: a comprehensive review of phase 3 candidates. *Npj Vaccines* **6**, 28 (2021).
16. Krammer, F. SARS-CoV-2 vaccines in development. *Nature* **586**, 516–527 (2020).
17. Thanh Le, T. *et al.* The COVID-19 vaccine development landscape. *Nat. Rev. Drug Discov.* **19**, 305–306 (2020).
18. Liang, C.-Y. *et al.* Imprinting of serum neutralizing antibodies by Wuhan-1 mRNA vaccines. *Nature* 1–3 (2024) doi:10.1038/s41586-024-07539-1.
19. Tortorici, M. A. *et al.* Persistent immune imprinting occurs after vaccination with the COVID-19 XBB.1.5 mRNA booster in humans. *Immunity* **57**, 904-911.e4 (2024).
20. Wang, Q. *et al.* Deep immunological imprinting due to the ancestral spike in the current bivalent COVID-19 vaccine. *Cell Rep. Med.* **4**, (2023).
21. Reynolds, C. J. *et al.* Immune boosting by B.1.1.529 (Omicron) depends on previous SARS-CoV-2 exposure. *Science* **377**, eabq1841 (2022).
22. Chemaitelly, H. *et al.* Long-term COVID-19 booster effectiveness by infection history and clinical vulnerability and immune imprinting: a retrospective population-based cohort study.

Lancet Infect. Dis. **23**, 816–827 (2023).
23. Wang, Z. *et al.* Memory B cell responses to Omicron subvariants after SARS-CoV-2 mRNA breakthrough infection in humans. *J. Exp. Med.* **219**, e20221006 (2022).
24. Wang, Q. *et al.* XBB.1.5 monovalent mRNA vaccine booster elicits robust neutralizing antibodies against XBB subvariants and JN.1. *Cell Host Microbe* **32**, 315-321.e3 (2024).
25. Johnston, T. S. *et al.* Immunological imprinting shapes the specificity of human antibody responses against SARS-CoV-2 variants. *Immunity* **57**, 912-925.e4 (2024).
26. Yisimayi, A. *et al.* Prolonged Omicron-specific B cell maturation alleviates immune imprinting induced by SARS-CoV-2 inactivated vaccine. *Emerg. Microbes Infect.* **13**, 2412623 (2024).
27. Chen, Y. *et al.* SARS-CoV-2 Omicron infection augments the magnitude and durability of systemic and mucosal immunity in triple-dose CoronaVac recipients. *mBio* **15**, e02407-23 (2024).
28. Yisimayi, A. *et al.* Repeated Omicron exposures override ancestral SARS-CoV-2 immune imprinting. *Nature* **625**, 148–156 (2024).
29. Yang, X. *et al.* Immune imprinting toward SARS-CoV-2 XBB: implications for vaccine strategy and variant risk assessment. *Signal Transduct. Target. Ther.* **10**, 372 (2025).
30. Tiller, T. *et al.* Efficient generation of monoclonal antibodies from single human B cells by single cell RT-PCR and expression vector cloning. *J. Immunol. Methods* **329**, 112–124 (2008).
31. Yuan, M. *et al.* Structural basis of a shared antibody response to SARS-CoV-2. *Science* https://doi.org/10.1126/science.abd2321 (2020) doi:10.1126/science.abd2321.
32. Wang, Y. *et al.* A large-scale systematic survey reveals recurring molecular features of public antibody responses to SARS-CoV-2. *Immunity* **55**, 1105-1117.e4 (2022).
33. Li L. *et al.* Breakthrough infection elicits hypermutated IGHV3-53/3-66 public antibodies with broad and potent neutralizing activity against SARS-CoV-2 variants including the emerging EG.5 lineages. *PLOS Pathog.* **19**, e1011856 (2023).
34. Vanshylla, K. *et al.* Discovery of ultrapotent broadly neutralizing antibodies from SARS-CoV-2 elite neutralizers. *Cell Host Microbe* **30**, 69-82.e10 (2022).
35. Yan, Q. *et al.* Germline IGHV3-53-encoded RBD-targeting neutralizing antibodies are commonly present in the antibody repertoires of COVID-19 patients. *Emerg. Microbes Infect.* **10**, 1097–1111 (2021).
36. Zhang, Q. *et al.* Potent and protective IGHV3-53/3-66 public antibodies and their shared escape mutant on the spike of SARS-CoV-2. *Nat. Commun.* **12**, 4210 (2021).
37. Nutalai, R. *et al.* Potent cross-reactive antibodies following Omicron breakthrough in vaccinees. *Cell* **185**, 2116-2131.e18 (2022).
38. Tan, T. J. C. *et al.* Sequence signatures of two public antibody clonotypes that bind SARS-CoV-2 receptor binding domain. *Nat. Commun.* **12**, 3815 (2021).
39. Jian, F. *et al.* Evolving antibody response to SARS-CoV-2 antigenic shift from XBB to JN.1. *Nature* 1–3 (2024) doi:10.1038/s41586-024-08315-x.
40. Lee, E.-C. *et al.* Complete humanization of the mouse immunoglobulin loci enables efficient therapeutic antibody discovery. *Nat. Biotechnol.* **32**, 356–363 (2014).
41. Cao, Y. *et al.* Omicron escapes the majority of existing SARS-CoV-2 neutralizing antibodies. *Nature* **602**, 657–663 (2022).
42. Jian, F. *et al.* Evolving antibody response to SARS-CoV-2 antigenic shift from XBB to JN.1.

Nature **637**, 921–929 (2025).
43. Cao, Y. *et al.* BA.2.12.1, BA.4 and BA.5 escape antibodies elicited by Omicron infection. *Nature* **608**, 593–602 (2022).
44. Cao, Y. *et al.* Imprinted SARS-CoV-2 humoral immunity induces convergent Omicron RBD evolution. *Nature* **614**, 521–529 (2023).
45. Jian, F. *et al.* Viral evolution prediction identifies broadly neutralizing antibodies to existing and prospective SARS-CoV-2 variants. *Nat. Microbiol.* 1–15 (2025) doi:10.1038/s41564-025-02030-7.
46. Lim, W. W., Mak, L., Leung, G. M., Cowling, B. J. & Peiris, M. Comparative immunogenicity of mRNA and inactivated vaccines against COVID-19. *Lancet Microbe* **2**, e423 (2021).
47. Xu, W., Wu, J. & Cao, L. COVID-19 pandemic in China: Context, experience and lessons. *Health Policy Technol.* **9**, 639–648 (2020).
48. Bo, W. *et al.* The current COVID-19 pandemic in China: An overview and corona data analysis. *Alex. Eng. J.* **61**, 1369–1381 (2022).
49. Gauffin K., Östergren O. & Cederström A. The global response to the pandemic: An empirical cluster analysis of policies targeting COVID-19. *PLOS ONE* **20**, e0322692 (2025).
50. Yanez Arteta, M. *et al.* Successful reprogramming of cellular protein production through mRNA delivered by functionalized lipid nanoparticles. *Proc. Natl. Acad. Sci.* **115**, E3351–E3360 (2018).
51. Li, H. *et al.* Establishment of replication-competent vesicular stomatitis virus-based recombinant viruses suitable for SARS-CoV-2 entry and neutralization assays. *Emerg. Microbes Infect.* **9**, 2269–2277 (2020).
52. Ye, J., Ma, N., Madden, T. L. & Ostell, J. M. IgBLAST: an immunoglobulin variable domain sequence analysis tool. *Nucleic Acids Res.* **41**, W34–W40 (2013).
53. Gupta, N. T. *et al.* Change-O: a toolkit for analyzing large-scale B cell immunoglobulin repertoire sequencing data. *Bioinformatics* **31**, 3356–3358 (2015).
54. Lin, S. G. *et al.* Highly sensitive and unbiased approach for elucidating antibody repertoires. *Proc. Natl. Acad. Sci.* **113**, 7846–7851 (2016).
55. Traag, V. A., Waltman, L. & van Eck, N. J. From Louvain to Leiden: guaranteeing well-connected communities. *Sci. Rep.* **9**, 5233 (2019).

Methods

Human serum and PBMC isolation

Blood samples were obtained from convalescent individuals who had received various vaccine platforms (detailed in Supplementary Table 1). The research protocol and the collection of human blood samples were approved by the Institutional Review Broad (IRB) of Shenzhen Institute of Advanced Science, Chinese Academy of Science (Ethics committee archiving no. SIAT-IRB-230715-H0667) and Beijing Ditan Hospital, Capital Medical University (Ethics committee

540 archiving no. DTEC-KY2024-112-01). All participants provided their agreement for the collection,
541 storage and use of their blood samples strictly for research purposes and the subsequent publication
542 of related data.

543 To isolate serum and PBMCs, whole blood was diluted 1:1 with PBS (Invitrogen, C10010500BT)
544 containing 2% (v/v) fetal bovine serum (FBS; Hyclone, SH30406.05) and separated by density
545 gradient centrifugation using Ficoll (Cytiva, 17-1440-03). The upper serum layer was collected,
546 aliquoted, and stored at or below -20°C. Before use in assays, serum samples were heat-inactivated
547 and assessed for neutralizing titres against SARS-CoV-2 variant spike-pseudotyped vesicular
548 stomatitis virus (VSV).

549 The PBMC layer was harvested from the interface and processed further. Following red blood cell
550 lysis (Invitrogen eBioscience 1X RBC Lysis Buffer, 00-4333-57) and washing, PBMCs were either
551 used immediately or cryopreserved in FBS with 10% (v/v) DMSO (Solarbio, D8371) for storage in
552 liquid nitrogen. All PBMC samples were transported on dry ice. For B cell isolation, cryopreserved
553 PBMCs were thawed in PBS supplemented with 5% (v/v) FBS. B cells were subsequently enriched
554 by immunomagnetic positive selection using the EasySep™ Human CD19 Positive Selection Kit II
555 (STEMCELL, 17854) following the manufacturer's protocol. The resulting purified B cells were
556 resuspended in PBS with 2% (v/v) FBS, and cell counts and viability were determined using 0.4%
557 (w/v) trypan blue staining (Invitrogen, T10282) on a Countess Automated Cell Counter (Invitrogen).

558 **Mice**

559 All animal experiments were conducted under protocols approved by the Animal Welfare Ethics
560 Committee of HFK Biologics (Approval No. HFK-AP-20250313). The humanized mouse model
561 (NeoMab-IgG), provided by NeoMab Biotechnology Co., Ltd., was created by in situ replacing the
562 mouse heavy chain variable region genes and kappa light chain variable region genes with human
563 genes in BALB/c mouse background. The mouse constant region genes were retained, making sure
564 the Fc of the immunoglobulins can interact with the Fc receptors expressed on other immune cells
565 normally, supporting standard immune system development and response. The IGHV3-53$^{+/+}$ or
566 IGHV3-53$^{+/-}$ mice were generated by Cyagen Biosciences (Suzhou, China). To generate this mice,
567 the targeting construct replaced the sequence from ATG start codon to exon 3 of mouse Ighv3-1 by

568 the sequence from ATG start codon to exon 2 of the human IGHV3-53, including the introns. The
569 Cas9 protein, construct and guide RNAs (gRNA-A1: 5'-TGAGAGTGCTGATTCTTTTGTGG-3',
570 gRNA-A2: 5'-TGCAGTGCTGCTCTGCAAGGAGG-3' and gRNA-B1: 5'-
571 TGGCTGTTCACAGCCTTTCCTGG-3', gRNA-B2: 5'-TGGTGCAGTGCTGCTCTGCAAGG-3')
572 were microinjected into zygotes from BALB/cAnCya wild-type mice. The embryos were
573 transferred to recipient female mice to obtain F0 mice. The genotype of IGHV3-53$^{+/+}$ or IGHV3-
574 53$^{+/-}$ mice was confirmed by PCR using two pairs of primers (F4: 5'-
575 CACCATCTCCAGAGACAATTCCAAG-3', R3: 5'-GTTCTGGATACCAATGTGCCTTCAG-3'
576 and F3: 5'-TGCAGTCAGTAGCCACCTCGCCAAT-3', R4: 5'-
577 CATCAGACAGGATACCTTCAGAGAAG-3') and sequencing. Mice of all strains (6–8 weeks old)
578 were housed under specific-pathogen-free (SPF) conditions, maintained at 22 ± 2°C with 50–60%
579 humidity on a 12-hour light/dark cycle. All animals had *ad libitum* access to standard chow and
580 sterile water.

581 **mRNA-LNP Synthesis and Formulation**

582 A PSP73 plasmid bearing the antigen insert followed by a 120-nt poly(T) tract was linearized with
583 the appropriate restriction enzyme. This DNA served as a template for *in vitro* transcription process
584 to generate RNA that encoded the SARS-CoV-2 Wuhan, BA.1, BA.5, XBB.1.5 and JN.1 S6P (F817P,
585 A892P, A899P, A942P, K986P, V987P, R683A and R685A) protein. Linearized DNA template (1
586 μg) was transcribed for 2 hours at 37°C using the EasyCap T7 Co-transcription Kit with CAG
587 Trimer (Vazyme, DD4203). Following transcription, the DNA template was digested by incubation
588 with 1 U of RNase-free DNase I for 15 minutes at 37°C. The resulting mRNA was purified with
589 VAHTS RNA Clean Beads (Vazyme, N412-03). The concentration and purity of the purified mRNA
590 were determined by UV spectrophotometry (absorbance at 260 nm and A260/A280), and its
591 integrity was verified by agarose gel electrophoresis.

592 The mRNA was encapsulated in a functionalized lipid nanoparticle (LNP) as described previously
593 [50]. The lipid mixture (oil phase) was prepared by dissolving SM-102, DSPC, cholesterol, and DMG-
594 PEG2000 in 100 % ethanol at a molar ratio of 50:10:38.5:1.5 to a total concentration of 9.04 mg/mL.
595 The filter-sterilized (0.22 μm) aqueous phase, consisting of 50 mM sodium citrate buffer (pH 4.0),
596 and the purified mRNA was diluted within it to a concentration of 133 μg/mL. Oil and aqueous

phases were then rapidly mixed at a 3:1 volume ratio using a staggered herringbone micromixer, operating at a total flow rate of 12 mL/min to induce LNP self-assembly. The crude LNP suspension underwent buffer exchange and purification via overnight dialysis at 4°C against a solution of 10 mM Tris-HCl (pH 7.4) with 8-10% (w/v) sucrose, using 10 kDa MWCO dialysis cassettes. The dialyzed LNPs were subsequently concentrated by centrifugation at 1,500-2,500 × g for 10-15 minutes at 4°C using 10 kDa MWCO ultrafiltration units (ULRC0100150P). The final formulation was adjusted to a sucrose concentration of 8.7% (w/v), aliquoted, flash-frozen in liquid nitrogen, and stored at -80°C.

The final product was subjected to rigorous quality control. Key attributes including particle size (by dynamic light scattering), RNA encapsulation efficiency (by RiboGreen assay), mRNA integrity (by capillary electrophoresis), osmolality, and endotoxin levels (by LAL assay) were assessed. All manufactured batches were required to meet the following release criteria: a particle diameter of 80-100 nm, ≥90% RNA encapsulation, ≥80% mRNA integrity, and an endotoxin level below 1 EU/mL.

Mouse immunization and passive antibody transfer

For immunization, mice were administered mRNA-LNP vaccines. The specific immunization regimens, including vaccine type, dosage, and timelines, are detailed in the schematics of Figure 2a, 5d, 6b, 6f and Extended Data figure 11a and 11c. On the day of administration, LNP-mRNA vials were thawed on ice and diluted in sterile 1× PBS to the appropriate concentration. Each mouse was injected intramuscularly (i.m.) into the quadriceps muscle with 100 μL of the vaccine solution using a 29 G insulin syringe. To prevent leakage of the inoculum, the needle was held in place for 3–5 seconds post-injection.

For passive antibody transfer, purified monoclonal antibodies (BD55-1205-mIgG1, BD55-1205-hIgG1, or BD57-2665-mIgG1) with low endotoxin levels (<0.02 EU/mg) were used. The antibodies were diluted in sterile PBS to the desired concentration for injection. Female BALB/c mice (6–8 weeks old) received a 200 μL dose via intraperitoneal (i.p.) injection in the left lower quadrant using a 26 G needle. Mice were monitored for at least 5 minutes following the injection, and any subsequent doses were administered according to the specified experimental schedules.

Pseudovirus preparation and neutralization assay

625 We generated SARS-CoV-2 variant spike protein pseudovirus as described previously [9–11,28,39,51].
626 Plasmids encoding a codon-optimized SARS-CoV-2 Spike (S) protein were constructed by inserting
627 the S gene into the pcDNA3.1 vector. To produce pseudovirus, 293T cells (ATCC, CRL-3216) were
628 transfected with the S protein expressing plasmids with Lipofectamine 3000 (Invitrogen, L3000015)
629 and subsequently infected with G*ΔG-VSV (Kerafast, EH1020-PM). After 24 hours, the
630 supernatant containing the pseudovirus was harvested, filtered through a 0.45 μm filter (Millipore),
631 aliquoted, and stored at -80°C.

632 Neutralization assays were performed using the Huh-7 cell line (JCRB, 0403). Monoclonal
633 antibodies or serum samples were serially diluted in DMEM (Hyclone, SH30243.01) and incubated
634 with the pseudovirus in 96-well plates for 1 hour at 37°C with 5% CO_2. Following incubation, Huh-
635 7 cells were seeded into the wells (2×10^4 cells per well) and cultured for an additional 24 hours at
636 37°C with 5% CO_2. To assess infection levels, the culture supernatant was removed and left 100 μ
637 l in each well. The Bright-Lite Luciferase Assay Substrate was reconstituted with its corresponding
638 Assay Buffer (Vazyme, DD1209-03-AB), and this mixture was added to the wells. After incubating
639 in the dark for 2 minutes, luminescence was measured using a microplate spectrophotometer
640 (PerkinElmer, HH3400). The NT_{50} or IC_{50} values were determined using a three-parameter logistic
641 regression model.

642 **Mouse tissue processing and B cell extraction**

643 Following euthanasia, the spleen, inguinal lymph nodes, and popliteal lymph nodes were harvested
644 and placed in RPMI 1640 culture medium (Invitrogen, C11875500CP) containing 5% (v/v) FBS.
645 Single-cell suspensions were prepared by mechanical disruption using the plunger of a syringe. The
646 popliteal and inguinal lymph nodes from each mouse were pooled, ground, and filtered through a
647 40 μm cell strainer. For the spleen, tissue was processed by the same grinding method and passed
648 through a 70 μm cell strainer, followed by centrifugation and lysis of red blood cells using 1× RBC
649 Lysis Buffer (Invitrogen eBioscience, 00-4333-57). After washing steps and centrifugation, the
650 resulting cell pellets were resuspended in PBS containing 2% (v/v) FBS.

651 Splenic B cells were enriched from the splenic single-cell suspensions via immunomagnetic
652 negative selection with the EasySep™ Mouse Pan-B Cell Isolation Kit (STEMCELL, 19844).

653 Following the manufacturer's protocol, the untouched, purified B cells were collected and washed
654 in PBS with 2% (v/v) FBS. The cell numbers of total lymph node cells and purified splenic B cells
655 were determined using 0.4% (w/v) trypan blue stain (Invitrogen, T10282) and a Countess
656 Automated Cell Counter (Invitrogen).

657 **Flow cytometry analysis and antigen-specific B cell sorting**

658 For the isolation of antigen-specific human B cells, enriched B cell populations from PBMCs were
659 prepared for fluorescence-activated cell sorting (FACS). The staining panel included FITC anti-
660 human CD20 (BioLegend, 302304), Brilliant Violet 605™ anti-human CD27 (BioLegend, 302824),
661 PE/Cyanine7 anti-human IgM (BioLegend, 314532), and PE/Cyanine7 anti-human IgD (BioLegend,
662 348210). Antigen-specific cells were detected using biotinylated JN.1 RBD (Sino Biological,
663 40592-V49H16-B) conjugated with PE-streptavidin (BioLegend, 405204) and APC-streptavidin
664 (BioLegend, 405207), and Wuhan RBD (Sino Biological, 40592-V27H-B) conjugated with BV421-
665 streptavidin (BioLegend, 405225). The viability dye 7-AAD (Invitrogen, 00-6993-50) was used to
666 exclude dead cells. A gating strategy was applied to sort single, viable (7-AAD^{-}), class-switched
667 (IgM^{-} and IgD^{-}), CD20^{+}CD27^{+} memory B cells that were positive for JN.1 RBD.

668 For the characterization of B cell responses in immunized mice, single-cell suspensions from the
669 inguinal and popliteal lymph nodes were stained for flow cytometry analysis. The cells were stained
670 with a panel including PE/Cyanine7 anti-mouse CD38 (BioLegend, 102718), Brilliant Violet 605™
671 anti-mouse/human B220 (BioLegend, 103244), APC/Cyanine7 anti-mouse IgD (BioLegend,
672 405716), Brilliant Violet 711™ anti-mouse IgM (BioLegend, 406539), and FITC anti-mouse/human
673 GL7 (BioLegend, 144603). The antigen probe cocktail consisted of biotinylated BA.5 RBD (Sino
674 Biological, 40592-V49H9-B) conjugated with PE- and APC-streptavidin, and Wuhan RBD
675 conjugated with BV421-streptavidin. Data for lymph node analysis were acquired on a Symphony
676 A5SE cytometer (BD Biosciences).

677 For the isolation of antigen-specific mouse splenic B cells, purified splenic B cells were stained
678 using the identical panel of antibodies and RBD probes as described for the lymph node analysis.
679 MoFlo Astrios EQ Cell Sorter (Beckman Coulter) was used for all sorting experiments, targeting
680 live (7-AAD^{-}), B220^{+}, CD38^{+}, class-switched (IgM^{-} and IgD^{-}), non-germinal center (GL7^{-}) B cells

681 that bound to the BA.5 RBD.

682 For all procedures, data were collected via Summit 6.0 software (Beckman Coulter). Data from all
683 experiments were uniformly analyzed using FlowJo v10.8 (BD Biosciences).

684 **Single-cell V(D)J sequencing**

685 For the 10X Genomics workflow, sorted antigen-specific B cells, suspended in PBS with 10% (v/v)
686 FBS, were processed with the Chromium Next GEM Single Cell V(D)J Reagent Kits v1.1 (10X
687 Genomics, CG000208). The cell suspension was loaded onto a 10X Chromium Controller to
688 generate Gel Beads-in-Emulsion (GEMs), which facilitate the barcoding of mRNA and subsequent
689 reverse transcription within individual droplets. Following cDNA synthesis, the product was
690 purified using a SPRIselect Reagent Kit (Beckman Coulter, B23318) and pre-amplified. Targeted
691 enrichment of paired V(D)J sequences was then achieved using 10X-specific BCR primers, and the
692 resulting products were used for sequencing library construction. These final libraries were
693 sequenced on an Illumina NovaSeq 6000 platform with a NovaSeq 6000 S4 Reagent Kit v1.5 (300
694 cycles; Illumina, 20028312). The 10X Genomics V(D)J Illumina sequencing data were assembled
695 as B cell receptor contigs and aligned to the B cell V(D)J reference using Cell Ranger (v.6.1.1)
696 pipeline. For human-source IGH and IGK contigs, we use GRCh38 as reference. For mouse-source
697 IGL contigs, we use GRCm38 as reference. Only the productive contigs and B cells with one heavy
698 chain and one light chain were kept to remove doublets. The germline V(D)J genes were identified
699 and annotated using IgBlast (v1.17.1) [52]. SHM nucleotides and residues in the antibody variable
700 domain were detected using Change-O toolkit (v.1.2.0) [53].

701 For the plate-based method, single antigen-specific B cells were sorted directly into the individual
702 wells of 96-well plates, each containing 4 μL of lysis buffer (0.095% Triton X-100, 2.5 μM oligo-
703 dT primer: 5'-
704 AAGCAGTGGTATCAACGCAGAGTACTTTTTTTTTTTTTTTTTTTTTTTTTTTTTVN-3',
705 2.5 mM dNTPs, 1 U/μL RNase Inhibitor). The plates were immediately processed by vortexing,
706 centrifugation, and incubation at 72°C for 3 min to denature RNA secondary structures, followed
707 by rapid chilling on ice. Reverse transcription was performed in each well by adding 5.7 μL of an
708 RT master mix (final concentrations: 1× HiScript III first-strand buffer, 10 U/μL HiScript III

709 reverse transcriptase, 2 U/μL RNase inhibitor, 5 mM DTT, 1 M betaine, 6 mM $MgCl_2$, 1 μM TSO
710 primer: 5'-AAGCAGTGGTATCAACGCAGAGTACATrGrG+G-3'). The RT reaction was
711 incubated at 37°C for 60 minutes, followed by enzyme inactivation at 85°C for 5 seconds. The
712 resulting cDNA served as a template for amplifying full-length immunoglobulin heavy and light
713 chain V(D)J sequences via a two-round nested PCR strategy using Phanta Max Master Mix (Vazyme,
714 P515). The first PCR round employed a multiplex primer pool targeting all VH, Vκ, and Vλ gene
715 families, along with constant region-specific reverse primers. A second, nested PCR round was then
716 performed with internal primers to enhance specificity and yield. Final amplicons were purified and
717 subsequently analyzed by Sanger sequencing. The germline V(D)J genes were identified and
718 annotated using IgBlast (v1.22.0) [52].

719 **HTGTS-Rep-seq**

720 0.5-4 μg of genomic DNA from purified splenic B cells was used for generating HTGTS-Rep-seq
721 libraries as previously described [54]. Four bait primers that target mouse JH1
722 (TGACATGGGGAGATCTGAGA), JH2 (CCCCAACAAATGCAGTAAAATCT), JH3
723 (GAGAATCTTGGTCCTGAAGGC), and JH4 (CTGCAATGCTCAGAAAACTCC) were mixed to
724 capture all heavy chain (HC) repertoire in one library. All primers carried a 5′ biotin modification
725 (5BiosG). These HTGTS-Rep-seq libraries were sequenced on an Illumina NextSeq platform (2 ×
726 150 bp paired-end) DNBSEQ-T7. Data were analyzed with the HTGTS-Rep-seq pipeline [54].

727 **Monoclonal antibody expression and purification**

728 The sequences for the antibody heavy and light chains were initially codon-optimized for expression
729 in human cells (GenScript). The variable regions (VH and VL) were then separately inserted into
730 corresponding expression vectors (pCMV3-CH, pCMV3-CL or pCMV3-CK). Plasmids of the
731 heavy and light chain constructs were transformed into *Escherichia coli* DH5α competent cells
732 (Tsingke, TSC-C01-96). After overnight incubation at 37°C, single colonies were picked for colony
733 PCR identification. Plasmid DNA of expanded cultures was extracted (CWBIO,CW2105) after
734 verified by Sanger sequencing.

735 For protein production, heavy and light chain plasmids were co-transfected into Expi293F cells
736 (Thermo Fisher, A14527) using polyethylenimine (PEI; Yeasen, 40816ES03). The plasmid-PEI

737 complexes were prepared in sterile 0.9% NaCl solution before being added to the cell culture. The
738 transfected cells were cultured at 36.5°C with 5% CO_2 and 175 rpm shaking for 6–10 days. A
739 nutrient supplement (OPM Biosciences, F081918-001) was added to each culture at 24 hours post-
740 transfection and every 48 hours thereafter.

741 To purify the antibodies, the culture supernatant was first clarified by centrifugation (3,000 × g, 10
742 minutes). The supernatant was then incubated with Protein A magnetic beads (GenScript, L00695)
743 for 2 hours to allow antibody binding. The beads were subsequently washed, and the bound
744 antibodies were eluted using a KingFisher automated purification system (Thermo Fisher). The
745 concentration of the purified antibody was determined using a NanoDrop spectrophotometer
746 (Thermo Fisher, 840-317400), and its purity was assessed by SDS-PAGE (LabLead, P42015).

747 **RBD depletion of serum**

748 To deplete RBD-specific antibodies from serum, 50 μL of Dynabeads™ MyOne™ Streptavidin T1
749 (Invitrogen, 65601) were washed once with PBS. 10 μg of biotinylated SARS-CoV-2 Wuhan RBD
750 was incubated with the washed beads for 1 hours with gentle rotation to allow binding via
751 streptavidin-biotin interaction. The beads were then collected using a magnetic rack for 2-3 min, the
752 supernatant was discarded, and the beads were washed three times with PBS to remove unbound
753 proteins. Subsequently, 200-400 μL of serum was incubated with the RBD-conjugated beads for
754 1 hours with gentle rotation to allow specific antibody binding. Finally, the tubes were placed on the
755 magnetic rack, and the supernatant representing the RBD-depleted serum was carefully collected
756 for downstream analyses.

757 **Enzyme-linked immunosorbent assays**

758 High-binding 96-well plates (NEST, 504201) were coated overnight at 4°C with SARS-CoV-2
759 Wuhan (Sino Biological, 40592-V27H-B) or BA.5 RBD proteins (Sino Biological, 40592-V49H9-
760 B). The following day, plates were washed three times with 1×PBST (Solarbio, P1033) and blocked
761 with 250 μL 3–5% bovine serum albumin (BSA; Solarbio, A8020) in 1×PBST for 2 hours at 37°C
762 to prevent non-specific binding. After three additional washes, 100 μL of serially diluted antibodies
763 or serum samples were added to the wells and incubated for 30 minutes at room temperature.
764 Unbound antibodies were removed by five washes with 1×PBST. Subsequently, 100 μL of HRP-

765 conjugated Goat anti-Mouse IgG (H+L) Cross-Adsorbed Secondary Antibody (Invitrogen, G21040)
766 was added and incubated for 30 minutes at room temperature. Following a final five washes, the
767 signal was developed by adding 100 μL of TMB substrate (Solarbio, PR1200) to each well and
768 incubating for 8 minutes in the dark. The reaction was terminated by adding 50 μL of stop solution
769 (Solarbio, C1058). The optical density (OD) was measured at 450 nm with a reference wavelength
770 of 630 nm using a Multiskan FC microplate reader (Thermo Scientific). Final absorbance values
771 were obtained by subtracting the OD630 reading from the OD450 reading for each well.

772 **Surface plasmon resonance**

773 Surface plasmon resonance (SPR) experiments were conducted using a Biacore 8K+ system (Cytiva)
774 at room temperature. For competitive binding assays, His-tagged SARS-CoV-2 BA.5 RBD protein
775 (5 μg/mL) was immobilized onto an anti-His-tagged CM5 sensor chip (Cytiva) for 1 minute.
776 Subsequently, a saturating concentration of the first antibody (Ab1, 20 μg/mL) was injected for 2
777 minutes, immediately followed by the injection of the second antibody (Ab2, 20 μg/mL) for another
778 2 minutes. The sensor surface was regenerated between cycles using a glycine solution (pH 1.5).
779 All binding data were recorded and processed using Biacore 8K Evaluation Software (v4.0.8.20368).
780 The degree of epitope competition was calculated using the following formula:

781 $$score_{\mathrm{Ab2-Ab1}} = 1 - \frac{response_{Ab2\ after\ Ab1}}{\overline{response_{Ab2\ alone}}}$$

782 Where $response_{Ab2\ after\ Ab1}$ represents the response units when Ab2 serves as the second
783 antibody and Ab1 as the first antibody, whereas $\overline{response_{Ab2\ alone}}$ denotes the mean response
784 units when Ab2 acts as the first antibody.

785 **DMS library construction**

786 Replicate deep mutational scanning (DMS) libraries of the SARS-CoV-2 BA.5 RBD (residues
787 N331–T531; Wuhan-Hu-1 numbering) were generated based on established protocols [28,41] with a
788 modification. Rather than using a pooled primer mix, we performed 201 individual PCR reactions,
789 each using a specific NNS primer pair to introduce all possible amino acid substitutions at a single
790 target residue. The resulting products from each single-site mutagenesis reaction were then
791 combined to form the final comprehensive library. Each unique RBD variant was subsequently

792 tagged with a distinct 26-nucleotide (N26) barcode via PCR. The mutagenized and barcoded RBD
793 sequences were then cloned into pETcon 2649 vector and the resulted plasmid libraries were
794 amplified in electrocompetent *E. coli* DH10B cells. The association between every RBD variant and
795 its corresponding N26 barcode was established by preparing PacBio sequencing libraries and
796 performing long-read sequencing on the Sequel II platform. Amplified DMS plasmid libraries were
797 transformed into *Saccharomyces cerevisiae* strain EBY100. Transformed yeast cells were initially
798 selected on SD-CAA agar plates. Positive clones were then expanded by culturing in SD-CAA liquid
799 media. The resulting comprehensive DMS yeast libraries were preserved by flash-freezing in liquid
800 nitrogen and stored at -80 °C.

801 **Magnetic beads-based antibody mutation escape profiling**

802 High-throughput mutation escape profiling for mAbs was performed using magnetic beads based
803 on previously established protocols [28,41]. DMS yeast libraries (Wuhan and BA.5) first underwent
804 functional pre-screening. Non-functional or misfolded RBD variants were removed using ACE2-
805 biotin conjugate (Sino Biological, 10108-H08H-B) bound to streptavidin magnetic beads (Thermo
806 Fisher, 11533D). ACE2-bound yeast cells were washed with PBS containing 0.1% (v/v) BSA,
807 released, expanded in SD-CAA liquid medium, and cryopreserved at -80°C as functional libraries.

808 For Antibody Escape Selection, thawed functional libraries were cultured overnight in SD-CAA
809 with shaking, then back-diluted into SG-CAA medium to induce RBD surface expression. Escape
810 variants of each mAb were isolated using a sequential selection strategy, with 2 rounds of negative
811 selection to deplete antibody-binding variants and 1 round of positive selection to capture the
812 antibody-escaping population using anti-c-Myc magnetic beads (Thermo Fisher, 88843). The final
813 sorted yeasts were washed, regrown overnight and subjected to plasmid extraction using a 96-well
814 kit (Coolaber, PE053). The unique N26 barcodes appended to each RBD variant were amplified by
815 PCR using extracted plasmid as template. PCR products were purified with Ampure XP beads
816 (Beckman Coulter, A63882) and subjected to high-throughput single-end sequencing (NextSeq
817 500/550 platforms or MGI200 platforms).

818 **Antibody DMS data analysis**

819 The raw sequencing data from the DMS were processed as previously described [28]. Specifically, the

barcode sequences detected from both the antibody-screened and reference libraries were aligned with a barcode-variant dictionary derived from PacBio sequencing data of the Wuhan and BA.5 DMS libraries using the alignparse (v.0.6.2) and dms_variants (v.1.4.3) tools. Ambiguous barcodes were excluded during the merging of yeast libraries. Only barcodes detected more than five times in the reference library were considered for further analysis. The escape score for a variant X, present in both the screened and reference libraries, was calculated as $F \times (n_{X,ab}/N_{ab})/(n_{X,ref}/N_{ref})$, where F is a scaling factor to normalize the scores to a 0–1 range, and n and N represent the numbers of detected barcodes for variant X and the total barcodes in the antibody-screened (ab) or reference (ref) samples, respectively. For antibodies subjected to DMS with multiple replicates using different mutant libraries, the final escape score for each mutation was averaged for subsequent analyses.

We used graph-based unsupervised clustering and embedding to assign an epitope group to each antibody and visualize them in a two-dimensional space. Initially, site escape scores (sum of mutation escape scores per residue) for each antibody were normalized to a sum of one, representing a distribution over RBD residues. The dissimilarity between two antibodies is defined based on the Pearson's correlation coefficient of their escape score vectors using numpy (v1.25.2). A k-nearest-neighbour graph was constructed using the python-igraph module (v.0.9.6), and Leiden clustering was applied to assign a cluster to each antibody [55]. Cluster names were manually annotated on the basis of the characteristic sites in the average escape profiles of each cluster, using the same nomenclature as our previously published DMS dataset [28]. To visualize the dataset in two dimensions, uniform manifold approximation and projection was performed based on the k-nearest-neighbour graph using umap-learn module (v.0.5.2), and figures were generated using R package ggplot2 (v.3.3.3).

To compute the average immune pressure or identify escape hotspots using a collection of mAb DMS profiles, we incorporating two types of weight to account for the impact of each mutation on neutralizing activity and codon constraints at each residue. For codon usage constraints, mutations inaccessible through single nucleotide changes were assigned a weight of zero, whereas others received a weight of 1.0. We used Wuhan/D614G (Wuhan-Hu-1 reference genome) and BA.4/5 (EPI_ISL_11207535) to define one-nucleotide-accessible amino acid mutations. Neutralizing activity weights were calculated as $-\log10\ (IC_{50})$, with IC_{50} values below 0.0005 or above 1.0

adjusted to 0.0005 or 1.0, respectively. Raw escape scores for each antibody were normalized by the maximum score across all mutants. The weighted score for each antibody and mutation was obtained by multiplying the normalized scores by the corresponding two weights, and the final mutation-specific weighted score was the sum of scores for all antibodies in the designated set, subsequently normalized to a 0–1 range. To visualize the calculated escape maps, sequence logos were generated using the Python module logomaker (v.0.8).

856 **Figure legends**

857 **Figure 1 | mRNA and inactivated vaccine priming induce distinct immune imprinting level.**

858 **a,** Schematic of the SARS-CoV-2-related immune histories and sampling time of the inactivated-
859 only and mRNA-vaccinated cohorts involved in this study. **b,** Representative flow cytometry dot
860 plots of cross-reactive memory B cells from individuals from the inactivated-only (top) and mRNA-
861 vaccinated (bottom) cohorts. APC, allophycocyanin; PE, phycoerythrin; BV421, Brilliant Violet
862 421. **c,** Scatter plots showing the proportion of cross-reactive memory B cells (left), JN.1-reactive
863 memory B cells (middle), and Wuhan-reactive memory B cells (right). **d,** Serum IgG midpoint titre
864 against Wuhan (left) or JN.1 (right) RBD before and after Wuhan RBD depletion. Statistical
865 significance of the fold-reduction in titres was assessed between two cohorts. Dashed lines indicate
866 the limit of detection (midpoint titre = 10). **e,** NAb response of the two cohorts against a panel of
867 SARS-CoV-2 variant pseudoviruses. Geometric mean titres (GMTs) are shown on the top. Dashed
868 lines indicate the limit of detection (NT_{50} = 10). **f,** Heavy chain V gene usage proportion of the two
869 cohorts. IGHV3-53 and IGHV3-66 were combined for analysis. Two-tailed Wilcoxon rank-sum
870 tests were used in **c-e**. $*P < 0.05$, $**P < 0.01$, $***P < 0.001$, $****P < 0.0001$; NS, not significant
871 ($P > 0.05$).

872 **Figure 2 | V(D)J humanized mice recapitulates severe SARS-CoV-2 imprinting.**

873 **a,** Schematic of the mouse immunization regimen and sampling timeline for wild-type and V(D)J-
874 humanized mice. The number of mice is indicated at the time point for each endpoint experiment.
875 **b,** Scatter plots showing the proportion of cross-reactive memory B cells in draining lymph nodes
876 of the two mouse strains after one (left) or two (right) BA.5 boosts. **c,** Serum IgG midpoint titre of
877 the two mouse strains after one (left) or two (right) BA.5 boosts against Wuhan or BA.5 RBD before
878 and after Wuhan RBD depletion. Statistical significance of the fold-reduction in titres was assessed
879 between humanized and wild-type mice. Dashed lines indicate the limit of detection (midpoint
880 titre = 100). **d,** Serum neutralization titres (NT_{50}) of the two mouse models after Wuhan priming
881 (left), one BA.5 boost (middle), or two BA.5 boosts (right) against a panel of SARS-CoV-2 variant
882 pseudoviruses. Geometric mean titres (GMTs) are shown on the top. Dashed lines indicate the limit
883 of detection (NT_{50} = 60). Two-tailed Wilcoxon rank-sum tests were used in **b-d**.

884 **Figure 3 | Distinct antibody landscapes between mRNA vaccinated humanized and wild-type**
885 **mice.**

886 **a–c**, Normalized average DMS escape scores for mAbs isolated from humanized (top) and wild-
887 type (bottom) mice following Wuhan priming (**a**), the first BA.5 booster (**b**), or the second BA.5
888 booster (**c**). Escape scores were aggregated and weighted by the IC_{50} of each individual mAb (To
889 focus on the neutralizing mAbs, lower IC_{50} corresponds to greater weight) against D614G for
890 Wuhan-primed groups or BA.5 for BA.5-boosted groups. Codon constraints were applied (see
891 Methods). In each panel, the ten residues with the highest cumulative escape scores are annotated,
892 with their specific mutational escape profiles visualized as logo plots above the scatter plots. To
893 highlight divergent immune pressure, residues exhibiting pronounced differences between
894 humanized and wild-type strains (as identified in Extended Data Fig. 6) are colored red in both the
895 scatter plots and logo plots.

896

897 **Figure 4 | VDJ germline difference shapes vaccination- induced SARS-CoV-2 antibody epitope**
898 **distribution.**

899 Epitope distribution of the antibody repertoire generated after Wuhan priming in humanized (**a**) and
900 wild-type mice (**b**). The Wuhan RBD structure (PDB: 6m0j) is displayed as a surface map colored
901 by normalized aggregate escape scores, with epitope groups outlined in distinct colors. Their
902 neutralizing category (Strong, Weak, or Non-neutralizing), antibody count, and percentage are
903 indicated. Key escape residues for each group are displayed as logos, and the sites with the highest
904 escape scores per group are labeled on the structure. Paired heavy and light chain V-gene usage for
905 each epitope is shown in Sankey plots. **c,** Pyramidal bar charts showing the proportional distribution
906 of epitope groups in antibodies isolated from humanized and wild-type mice after Wuhan priming
907 and after one or two BA.5 boosts. Bars are colored according to the log10 geometric mean IC_{50} of
908 antibodies within each group.

909 **Figure 5 | IGHV3-53/66-encoded Class 1 antibody drives SARS-CoV-2 imprinting through**
910 **epitope masking.**

911 **a,** Donut plots showing the cross-reactivity of A1 antibodies from humanized or wild-type mice.

912 The number of antibodies are indicated in the centre of the donut. **b,** Heatmap of competitive SPR
913 for various antibody groups. The definition of the competition score is described in the Methods
914 section. **c,** Schematic of the molecular mechanism by which pre-existing IGHV3-53/66-encoded A1
915 antibodies cause strong immune imprinting. **d,** Schematic of the antibody passive transfer
916 experiment. Timing of mRNA vaccinations, antibody injection, blood collection, and FACS analysis
917 are indicated. Mice were divided into experimental groups (receiving 400 μg BD55-1205-hIgG1,
918 200 μg BD55-1205-hIgG1, or 200 μg BD55-1205-mIgG1) and control groups (receiving 200 μg
919 BD57-2665-mIgG1 or PBS). The number of mice per group is indicated at the endpoint. **e,** DMS
920 escape map logoplots for BD55-1205 and BD57-2665 and their projection onto the SARS-CoV-2
921 Wuhan RBD (PDB: 6m0j). **f,** Scatter plots showing the proportion of cross-reactive memory B cells
922 in draining lymph nodes after one (left) or two (right) BA.5 boosts. **g,** Scatter plots showing the
923 proportion of cross-reactive germinal center B cells in draining lymph nodes after one BA.5 boost.
924 **h,** Serum IgG midpoint titre against BA.5 RBD before and after Wuhan RBD depletion. Statistical
925 significance of the fold-reduction in titres was assessed between groups. Dashed lines indicate the
926 limit of detection (midpoint titre = 100). Two-tailed Wilcoxon rank-sum tests were used in **f-h**.

927 **Figure 6 | IGHV3-53 knock-in mouse faithfully reflects SARS-CoV-2 antibody map in human.**

928 **a,** Usage percentage of IGHV3-53 and Ighv3-1 in naïve B cells from HTGTS sequencing of IGHV3-
929 $53^{+/+}$ (balb/c), IGHV3-$53^{+/-}$ (balb/c* C57B6/J), and wild-type (C57B6/J) mice. **b,** Schematic of the
930 immunization regimen and time points for blood collection and FACS analysis of the three mouse
931 models involved in this study. The number of mice is indicated above the timeline. **c,** Scatter plots
932 showing the proportion of cross-reactive memory B cells in draining lymph nodes of the three mouse
933 models after two BA.5 boosts. **d,** Serum IgG midpoint titre of the three mouse strains after two BA.5
934 boosts against BA.5 RBD before and after Wuhan RBD depletion. Statistical significance of the
935 fold-reduction in titres was assessed between groups. Dashed lines indicate the limit of detection
936 (midpoint titre = 100). **e,** Serum neutralization titres (NT_{50}) of the three mouse strains after one (left)
937 or two (right) BA.5 boosts against a panel of SARS-CoV-2 variant pseudoviruses. Geometric mean
938 titres (GMTs) are shown on the top. Dashed lines indicate the limit of detection (NT_{50} = 60). **f,**
939 Schematic of the immunization regimen simulating real-world SARS-CoV-2 exposure history. **g,**
940 Serum neutralization titres (NT_{50}) of IGHV3-$53^{+/+}$ and wild-type mice against a panel of SARS-

941 CoV-2 variant pseudoviruses. Geometric mean titres (GMTs) are shown on the top. Dashed lines
942 indicate the limit of detection (NT_{50} = 180). **h,** Antigenic cartography was performed using mouse
943 (top) and human (bottom) serum neutralization data. Each square indicates a serum sample, and
944 each circle indicates a SARS-CoV-2 variant. Two-tailed Wilcoxon rank-sum tests were used in **c-e**
945 and **g**.

946 **Extended Data Figure 1 | Different epidemiological landscape of XFG and NB.1.8.1 in 2025.**

947 **a,** Prevalence of XFG and NB.1.8.1 in China and the rest of the world as of October 5, 2025. The
948 asterisk (*) denotes the specific lineage and its sublineages. Data were retrieved from CovSpectrum
949 (https://cov-spectrum.org/).

950 **Extended Data Figure 2 | Enrichment of IGHV3-53/66 and high SHM rate characterize the**
951 **mRNA-imprinted antibody repertoire.**

952 **a,** Clonal analysis of memory B cells from individuals in the mRNA-vaccinated cohort. Single
953 clones are colored white. The numbers of B cells analyzed are labelled in the centre of the donut
954 plots. **b,** Paired heavy and light chain V-gene usage for memory B cells from the mRNA-vaccinated
955 and inactivated-only cohorts. **c, d,** Violin plots comparing somatic hypermutation (SHM) rates
956 between the two cohorts, shown for heavy and light chains (**c**) and representative heavy chain V-
957 genes (**d**). The number of sequences (n) is indicated above each plot. Two-tailed Wilcoxon rank-
958 sum tests were used in **d**.

959 **Extended Data Figure 3 | V(D)J-humanized mice exhibit a cellular imprinting phenotype**
960 **dominated by cross-reactive GC and memory B cells.**

961 **a-c,** Scatter plots showing the proportion of cross-reactive B cells (**a**), total GC B cells (**b**), and
962 class-switched memory B cells (**c**). The indicated percentages reflect the frequency relative to
963 their respective parental gates defined in Supplementary Information Fig. 1b. **d,** Linear regression
964 analysis of the correlation between memory B cell cross-reactivity proportion and BA.5-specific
965 IgG titre.

966 **Extended Data Figure 4 | Repeated Omicron boosters fail to elicit robust Omicron-specific**
967 **neutralization in imprinted humanized mice.**

968 **a,** Line plots showing longitudinal pseudovirus neutralization titres (NT_{50}) against a panel of
969 SARS-CoV-2 variants in paired humanized and wild-type mice across Wuhan priming and BA.5
970 booster timepoints; lines connect data from the same mouse. Dashed lines indicate the limit of
971 detection ($NT_{50} = 60$). Two-tailed Wilcoxon rank-sum tests were used.

972 **Extended Data Figure 5 | Neutralization potency and cross-reactivity of mAbs from**
973 **humanized and wild-type mice.**

974 **a,b,** Comparison of antibody IC_{50} values against D614G and BA.5(**a**) and cross-reactivity
975 proportion (**b**) from humanized and wild-type mice. Two-tailed Wilcoxon rank-sum tests were
976 used in **a**.

977 **Extended Data Figure 6 | Differential escape hotspots in humanized versus wild-type mice.**

978 **a–c**, Scatter plots comparing the normalized average DMS escape scores of neutralizing
979 antibodies isolated from humanized (y-axis) versus wild-type (x-axis) mice following Wuhan
980 priming (**a**), the first BA.5 booster (**b**), and the second BA.5 booster (**c**). Residues falling along the
981 diagonal (y=x) indicate shared immune pressure between the two models. To identify divergent
982 hotspots—including those with low-to-moderate scores in one strain that are absent in the other—
983 a shaded tolerance region was defined by the boundaries $y = 1.4x + 0.3$ and $y = 0.6x - 0.18$. Points
984 falling outside this shaded region represent distinct escape hotspots. Among these outliers, the five
985 residues with the highest escape scores in each group are highlighted in red. Related to Fig. 3.

986 **Extended Data Figure 7 | Distinct SARS-CoV-2 antibody epitope distribution after**
987 **sequential BA.5 boosts.**

988 **a-d,** Epitope distribution of the antibody repertoire generated after one BA.5 boost (**a, b**) or two
989 BA.5 boosts (**c, d**) in humanized mice (**a, c**) and wild-type mice (**b, d**). Related to Figure 4. **e,**
990 Pyramidal bar charts showing the proportional distribution of epitope groups in antibodies isolated

991 from humanized and wild-type mice after one or two BA.5 boosts. Bars are colored according to
992 the log10 geometric mean IC_{50} of antibodies within each group.

993 **Extended Data Figure 8 | Pharmacokinetics and dose-dependent suppressive effects of**
994 **antibodies used in passive transfer.**

995 **a,** Schematic of the *in vivo* monoclonal antibody pharmacokinetic study. **b,** Serum IgG titres over
996 time following antibody injection (mIgG1 forms were detected using an anti-mouse Fc secondary
997 antibody, and hIgG1 forms using an anti-human Fc secondary antibody). Dashed lines indicate the
998 limit of detection (midpoint titre = 100). **c,** Schematic of the BD55-1205 dose-ranging experiment.
999 **d,** Corresponding serum IgG titres before and after Wuhan RBD depletion. Statistical significance
1000 of the fold-reduction in titres was assessed between groups. Dashed lines indicate the limit of
1001 detection (midpoint titre = 100). Two-tailed Wilcoxon rank-sum tests were used in **d**.

1002 **Extended Data Figure 9 | IGHV3-53 knock-in mice exhibit diminished Omicron**
1003 **neutralization boosting compared to wild-type mice.**

1004 **a,** Line plots showing longitudinal pseudovirus neutralization titres (NT_{50}) against a panel of
1005 SARS-CoV-2 variants in paired IGHV3-53$^{+/+}$ (top), IGHV3-53$^{+/-}$ (middle), and wild-type (bottom)
1006 mice across BA.5 booster timepoints; lines connect data from the same mouse. Dashed lines
1007 indicate the limit of detection (NT_{50} = 60). Two-tailed Wilcoxon rank-sum tests were used.

1008 **Extended Data Figure 10 | Strong back-boosting of Wuhan immunity in IGHV3-53 KI mice**
1009 **restricts the breadth of neutralization against emerging variants.**

1010 **a,** Serum neutralization titres (NT_{50}) of IGHV3-53$^{+/+}$ and wild-type mice against a panel of SARS-
1011 CoV-2 variant pseudoviruses following the fifth dose (XBB.1.5). Geometric mean titres (GMTs) are
1012 shown on the top. Dashed lines indicate the limit of detection (NT_{50} = 180). **b,** Radar plot illustrating
1013 the back-boosting effect of the JN.1 booster on neutralization titres against pre-JN.1 variants. **c,**
1014 Neutralization profiles of IGHV3-53$^{+/+}$ and wild-type mice following XBB.1.5 and JN.1 boosters.
1015 Fold changes and statistical significance between highlighted variants are indicated. Lines connect
1016 data from the same mouse. Two-tailed Wilcoxon rank-sum tests were used in **a-c**.

Extended Data figure 1

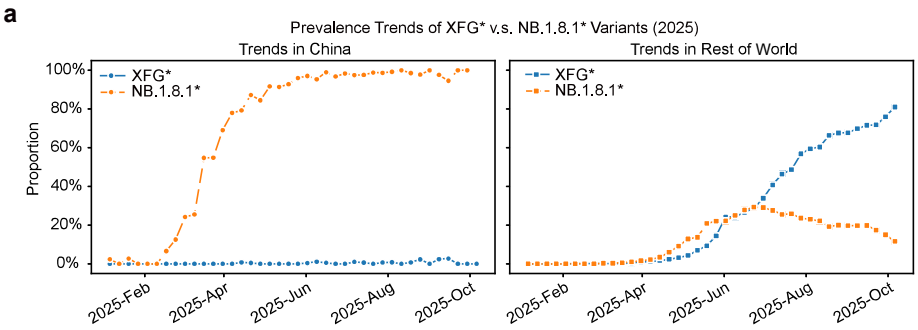

Extended Data Figure 1 | Different epidemiological landscape of XFG and NB.1.8.1 in 2025.
a, Prevalence of XFG and NB.1.8.1 in China and the rest of the world as of October 5, 2025. The asterisk (*) denotes the specific lineage and its sublineages. Data were retrieved from CovSpectrum (https://cov-spectrum.org/).

Extended Data figure 2

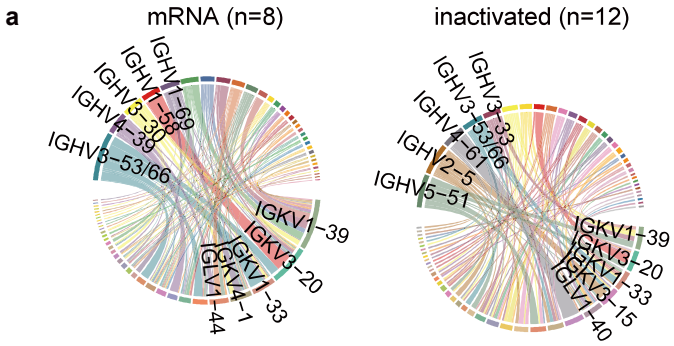

Extended Data Figure 2 | Paired heavy and light chain V-gene usage for human memory B cells
a, Paired heavy and light chain V-gene usage for memory B cells from the mRNA-vaccinated and inactivated-only cohorts.

Extended Data figure 3

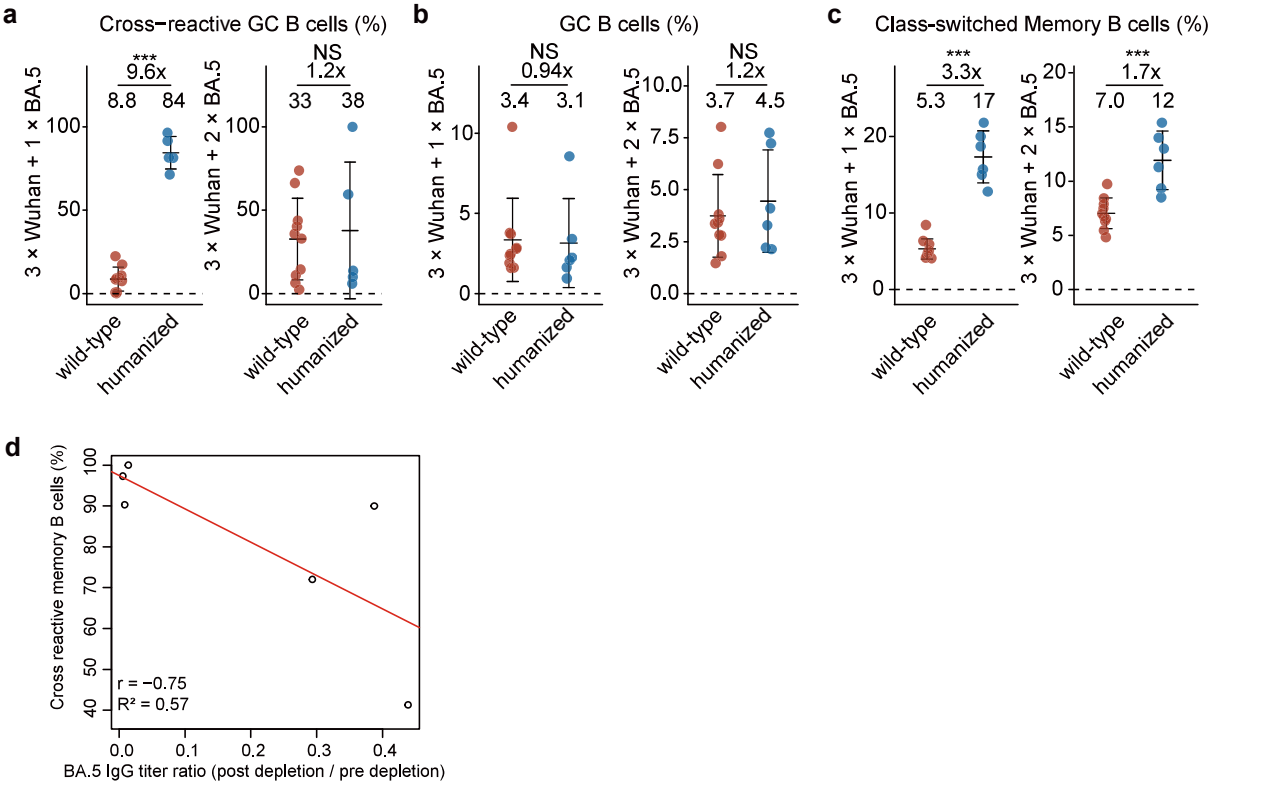

Extended Data Figure 3 | V(D)J-humanized mice exhibit a cellular imprinting phenotype dominated by cross-reactive GC and memory B cells.
a-c, Scatter plots showing the proportion of cross-reactive B cells (a), total GC B cells (b), and class-switched memory B cells (c). The indicated percentages reflect the frequency relative to their respective parental gates defined in Supplementary Information Fig. 1b. d, Linear regression analysis of the correlation between memory B cell cross-reactivity proportion and BA.5-specific IgG titer.

Extended Data figure 4

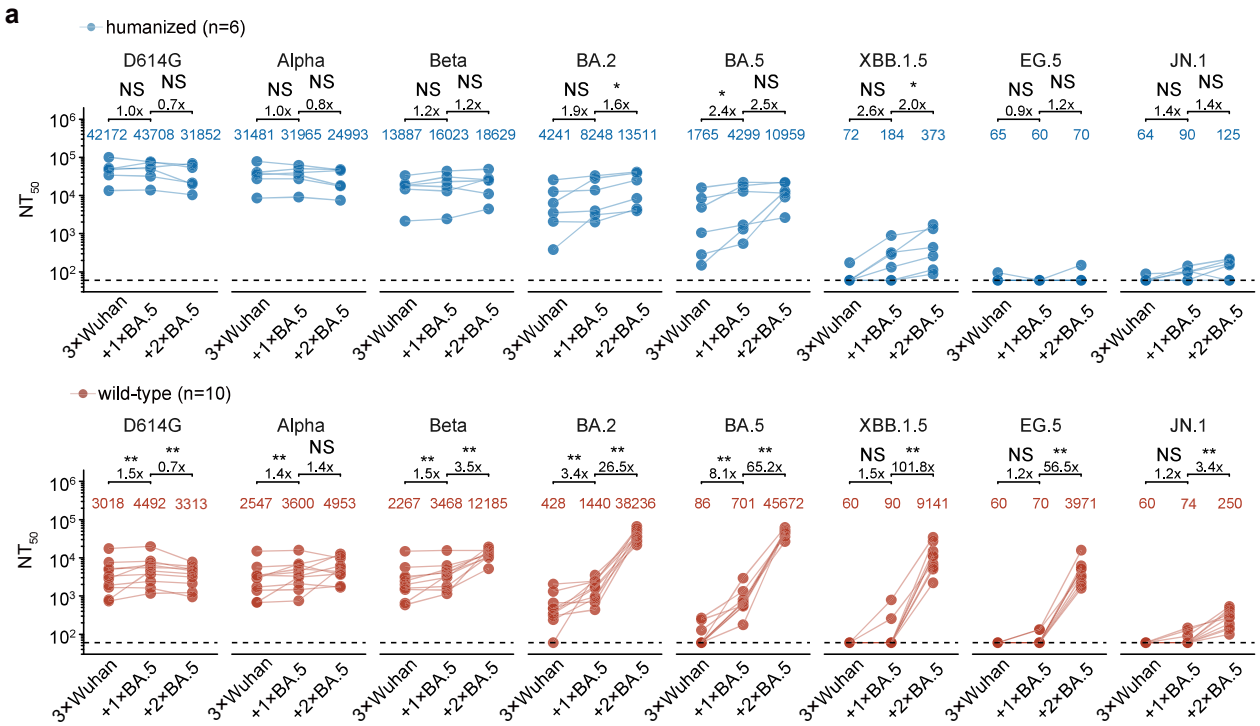

Extended Data Figure 4 | Repeated Omicron boosters fail to elicit robust Omicron-specific neutralization in imprinted humanized mice.
a, Line plots showing longitudinal pseudovirus neutralization titers (NT50) against a panel of SARS-CoV-2 variants in paired humanized and wild-type mice across Wuhan priming and BA.5 booster timepoints; lines connect data from the same mouse. Dashed lines indicate the limit of detection (NT50 = 60). Two-tailed Wilcoxon rank-sum tests were used.

Extended Data figure 5

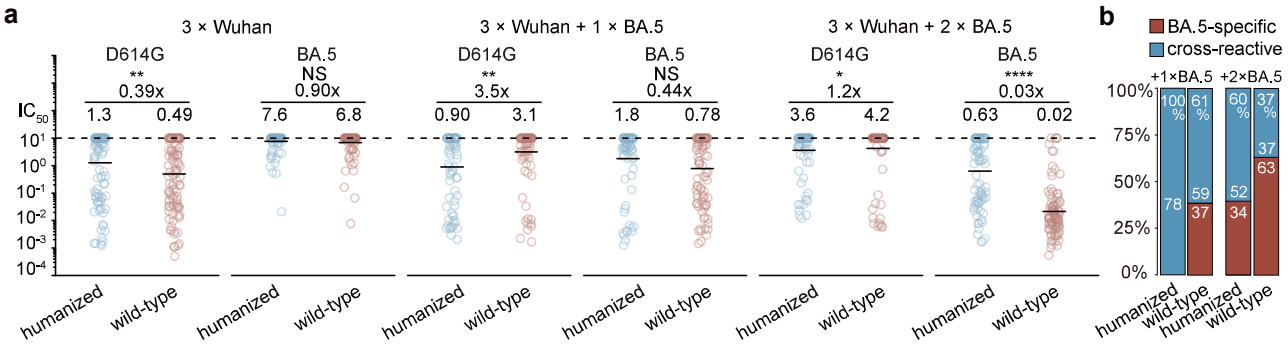

Extended Data Figure 5 | Neutralization potency and cross-reactivity of mAbs from humanized and wild-type mice.
a,b, Comparison of antibody IC50 values against D614G and BA.5(a) and cross-reactivity proportion (b) from humanized and wild-type mice. Two-tailed Wilcoxon rank-sum tests were used in a.

Extended Data figure 6

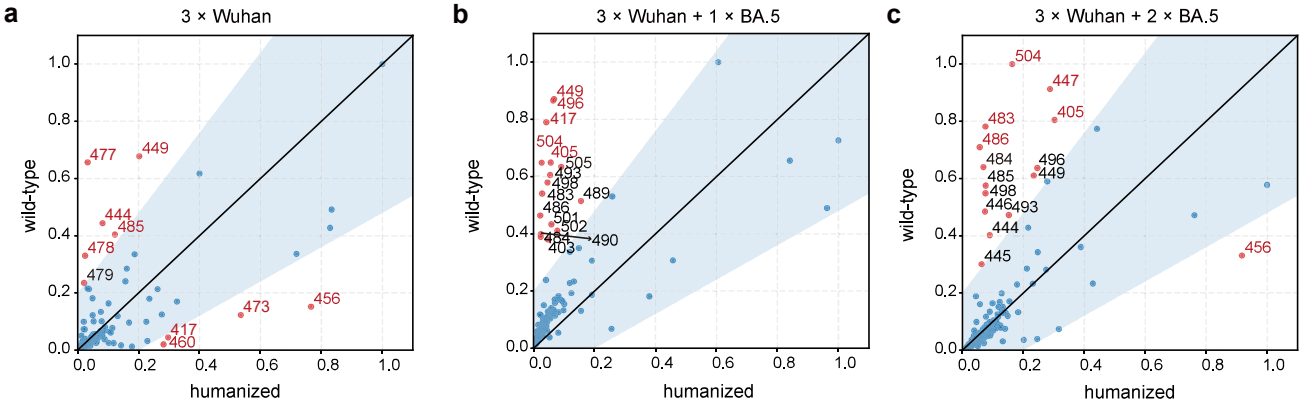

Extended Data Figure 6 | Differential escape hotspots in humanized versus wild-type mice.
a–c, Scatter plots comparing the normalized average DMS escape scores of neutralizing antibodies isolated from humanized (y-axis) versus wild-type (x-axis) mice following Wuhan priming (a), the first BA.5 booster (b), and the second BA.5 booster (c). Residues falling along the diagonal (y=x) indicate shared immune pressure between the two models. To identify divergent hotspots—including those with low-to-moderate scores in one strain that are absent in the other—a shaded tolerance region was defined by the boundaries y = 1.4x + 0.3 and y = 0.6x - 0.18. Points falling outside this shaded region represent distinct escape hotspots. Among these outliers, the five residues with the highest escape scores in each group are highlighted in red. Related to Fig. 3.

Extended Data figure 7

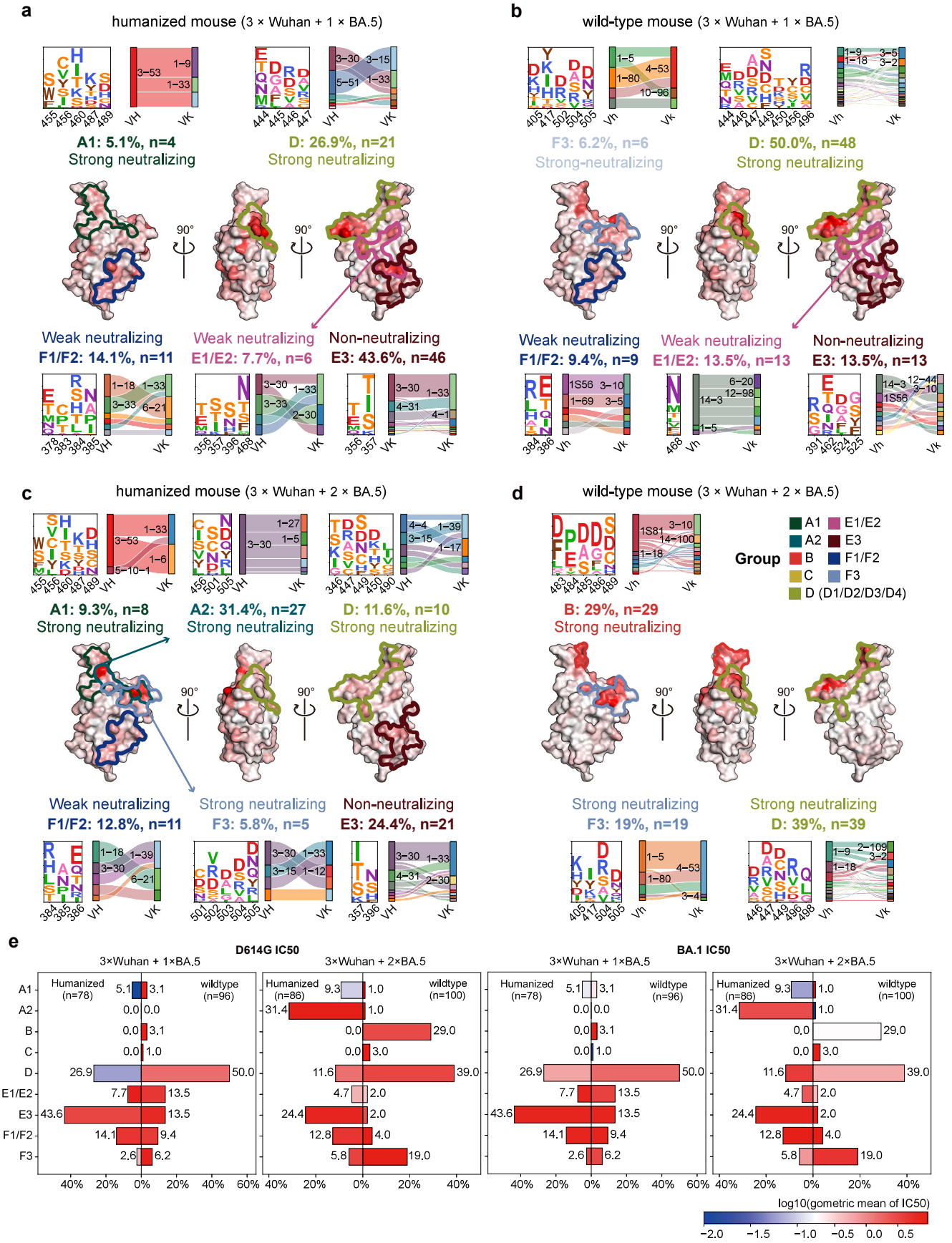

Extended Data Figure 7 | Distinct SARS-CoV-2 antibody epitope distribution after sequential BA.5 boosts.
a-d, Epitope distribution of the antibody repertoire generated after one BA.5 boost (a, b) or two BA.5 boosts (c, d) in humanized mice (a, c) and wild-type mice (b, d). Related to Figure 4. e, Pyramidal bar charts showing the proportional distribution of epitope groups in antibodies isolated from humanized and wild-type mice after one or two BA.5 boosts. Bars are colored according to the log10 geometric mean IC50 of antibodies within each group.

Extended Data figure 8

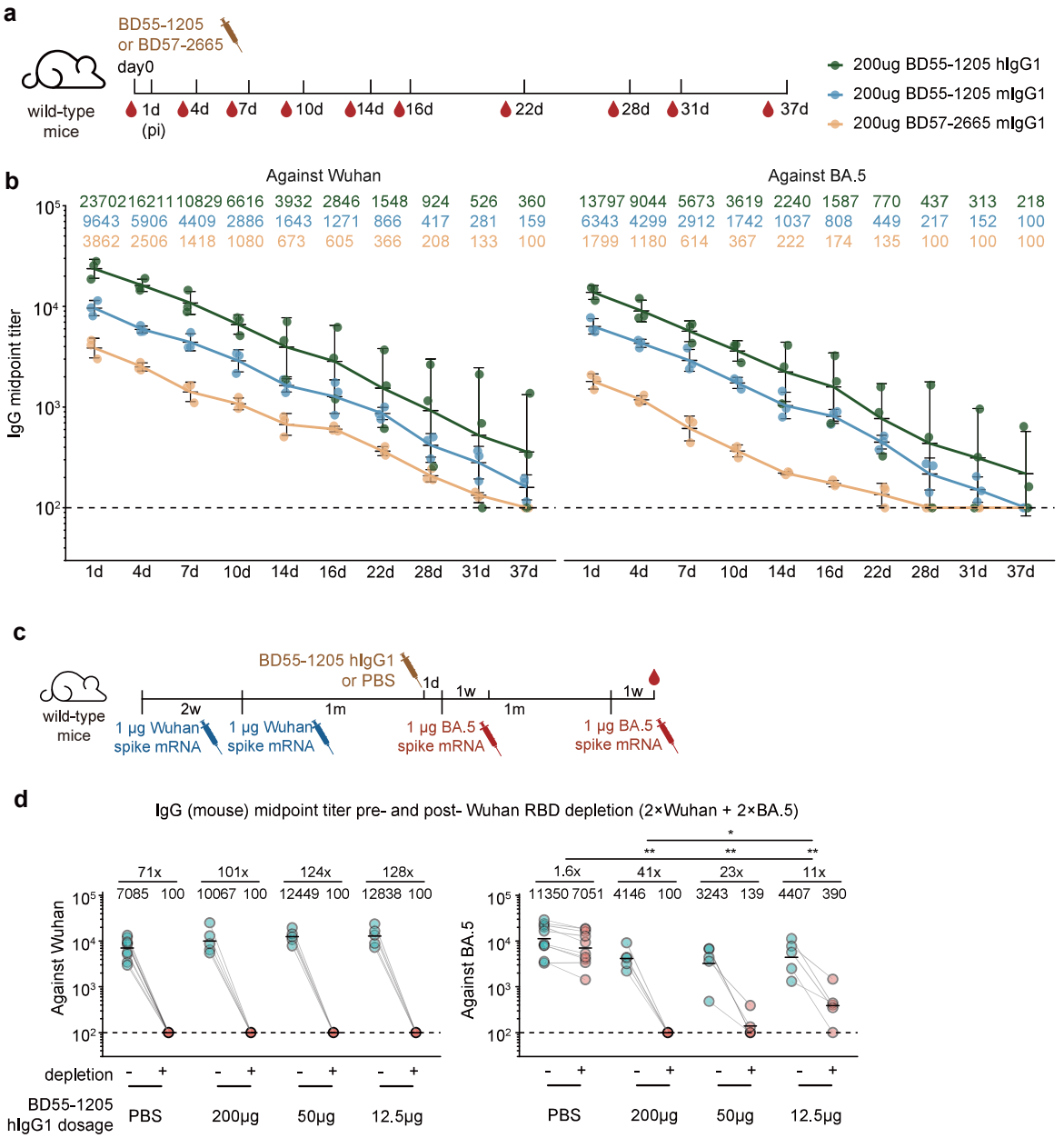

Extended Data Figure 8 | Pharmacokinetics and dose-dependent suppressive effects of antibodies used in passive transfer. a, Schematic of the in vivo monoclonal antibody pharmacokinetic study. b, Serum IgG titers over time following antibody injection (mIgG1 forms were detected using an anti-mouse Fc secondary antibody, and hIgG1 forms using an anti-human Fc secondary antibody). Dashed lines indicate the limit of detection (midpoint titre = 100). c, Schematic of the BD55-1205 dose-ranging experiment. d, Corresponding serum IgG titers before and after Wuhan RBD depletion. Statistical significance of the fold-reduction in titers was assessed between groups. Dashed lines indicate the limit of detection (midpoint titre = 100). Two-tailed Wilcoxon rank-sum tests were used in d.

Extended Data figure 9

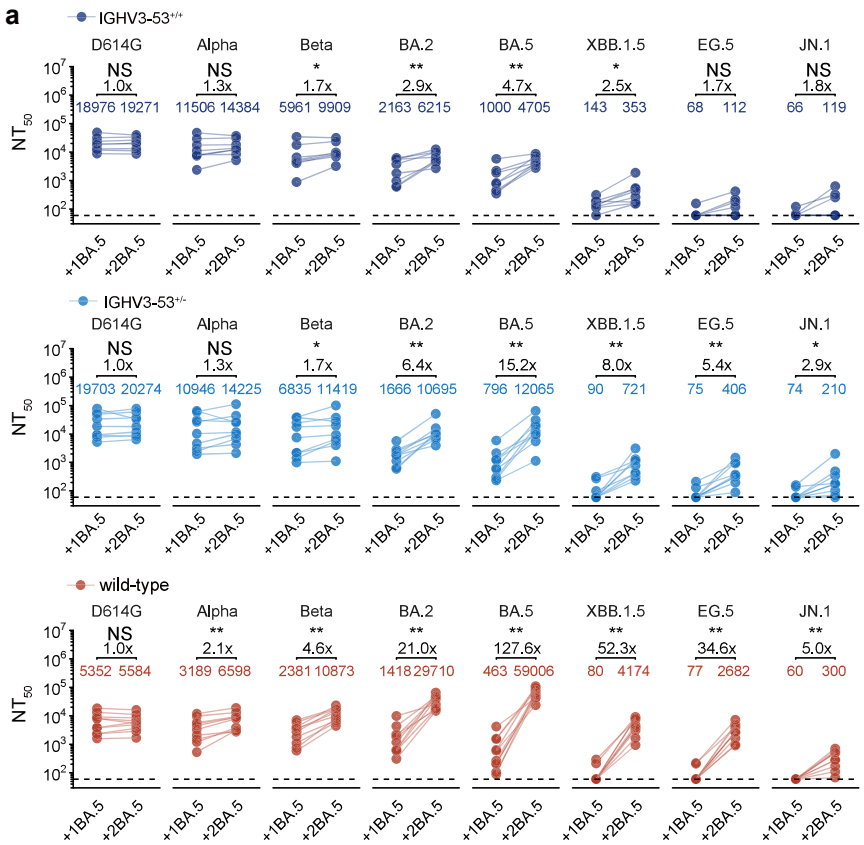

Extended Data Figure 9 | IGHV3-53 knock-in mice exhibit diminished Omicron neutralization boosting compared to wild-type mice.

a, Line plots showing longitudinal pseudovirus neutralization titers (NT50) against a panel of SARS-CoV-2 variants in paired IGHV3-53+/+ (top), IGHV3-53+/- (middle), and wild-type (bottom) mice across BA.5 booster timepoints; lines connect data from the same mouse. Dashed lines indicate the limit of detection (NT50 = 60). Two-tailed Wilcoxon rank-sum tests were used.

Extended Data figure 10

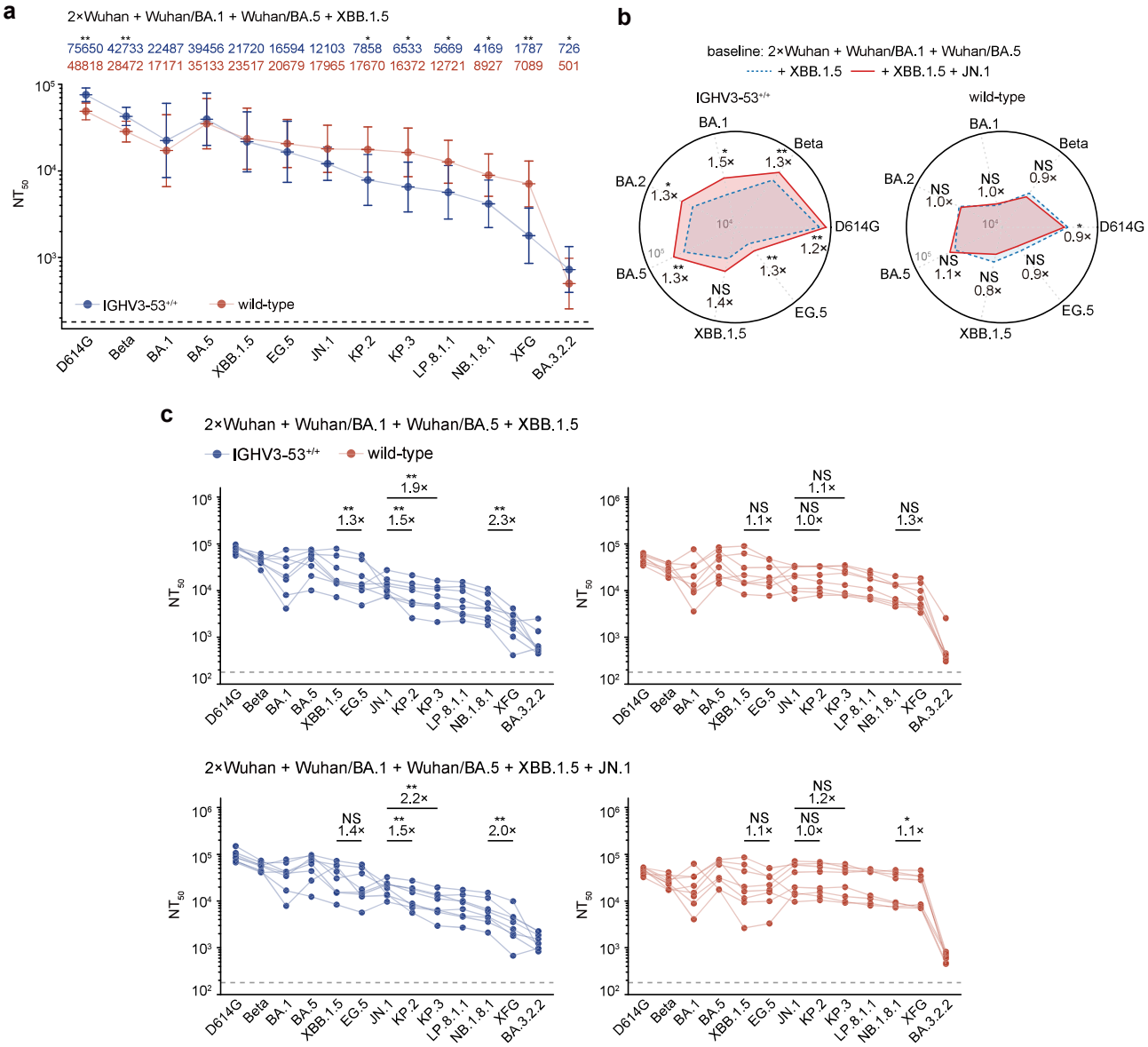

Extended Data Figure 10 | Strong back-boosting of Wuhan immunity in IGHV3-53 KI mice restricts the breadth of neutralization against emerging variants.
a, Serum neutralization titers (NT50) of IGHV3-53+/+ and wild-type mice against a panel of SARS-CoV-2 variant pseudoviruses following the fifth dose (XBB.1.5). Geometric mean titres (GMTs) are shown on the top. Dashed lines indicate the limit of detection (NT50 = 180). b, Radar plot illustrating the back-boosting effect of the JN.1 booster on neutralization titers against pre-JN.1 variants. c, Neutralization profiles of IGHV3-53+/+ and wild-type mice following XBB.1.5 and JN.1 boosters. Fold changes and statistical significance between highlighted variants are indicated. Lines connect data from the same mouse. Two-tailed Wilcoxon rank-sum tests were used in a-c.